

# Mapping global leaf inclination angle (LIA) based on field measurement data

Sijia Li<sup>1,2,3</sup>, Hongliang Fang<sup>2,3</sup>

<sup>1</sup>National-Local Joint Engineering Laboratory of Geo-Spatial Information Technology, Hunan University of Science and Technology, Xiangtan 411201, China

<sup>2</sup>LREIS, Institute of Geographic Sciences and Natural Resources Research, Chinese Academy of Sciences, Beijing 100101, China

<sup>3</sup>College of Resources and Environment, University of Chinese Academy of Sciences, Beijing 100049, China

Correspondence to: Sijia Li (lisj.19b@igsrr.ac.cn)

**Abstract.** Leaf inclination angle (LIA), the angle between leaf surface normal and zenith directions, is a vital trait in radiative transfer, rainfall interception, evapotranspiration, photosynthesis, and hydrological processes. Due to the difficulty in obtaining large-scale field measurement data, LIA is typically assumed to follow the spherical leaf distribution or simply considered constant for different plant types. However, the appropriateness of these simplifications and the global LIA distribution are still unknown. This study compiled global LIA measurements and generated the first global 500 m mean LIA (MLA) product by gap-filling the LIA measurement data using a random forest regressor. Different generation strategies were employed for noncrops and crops. The MLA product was evaluated by validating the nadir leaf projection function ( $G(0)$ ) derived from the MLA product with high-resolution reference data. The global MLA is  $41.47^\circ \pm 9.55^\circ$ , and the value increases with latitude. The MLAs for different vegetation types follow the order of cereal crops ( $54.65^\circ$ ) > broadleaf crops ( $52.35^\circ$ ) > deciduous needleleaf forest ( $50.05^\circ$ ) > shrubland ( $49.23^\circ$ ) > evergreen needleleaf forest ( $47.13^\circ$ )  $\approx$  grassland ( $47.12^\circ$ ) > deciduous broadleaf forest ( $41.23^\circ$ ) > evergreen broadleaf forest ( $34.40^\circ$ ). Cross-validation shows that the predicted MLA presents a medium consistency ( $r = 0.75$ ,  $RMSE = 7.15^\circ$ ) with the validation samples for noncrops, whereas crops show relatively lower correspondence ( $r = 0.48$  and  $0.60$  for broadleaf crops and cereal crops) because of limited LIA measurements and strong seasonality. The global  $G(0)$  distribution is opposite to that of the MLA and agrees moderately with the reference data ( $r = 0.62$ ,  $RMSE = 0.15$ ). This study shows that the common spherical and constant LIA assumptions may underestimate the intercept capability for most vegetation. The MLA and  $G(0)$  products derived in this study would enhance our knowledge about global LIA and should greatly facilitate remote sensing retrieval and land surface modeling studies.

The global MLA and  $G(0)$  products can be accessed at:

Li, S. and Fang, H. 2024, <https://doi.org/10.5281/zenodo.12739662>.

## 31 1 Introduction

32 Vegetation regulates terrestrial carbon and water cycles through a series of biophysical processes such as photosynthesis,  
33 respiration, and transpiration ([Foley et al., 1996](#); [Chen et al., 2019](#)). These biophysical processes are mainly carried by leaves  
34 and the characterization of leaves within canopies is vital for remote sensing and earth system modeling ([Ross, 1975](#);  
35 [Lawrence et al., 2019](#)). Leaf inclination angle (LIA) denotes the inclination of the leaf or needle to the horizontal plane or the  
36 angle between the leaf surface normal and zenith ([Wilson, 1960](#)). LIA is a key canopy structural trait that determines  
37 radiative transfer, rainfall interception, evapotranspiration, photosynthesis, and hydrological processes ([Sellers, 1985](#); [Ross,](#)  
38 [1981](#); [Mantilla-Perez and Salas Fernandez, 2017](#); [Xiao et al., 2000](#); [Maes and Steppe, 2012](#)). LIA has been used in radiative  
39 transfer modeling (RTM), remote sensing inversion, and land surface modeling (LSM) studies ([Tang et al., 2016](#); [Wang and](#)  
40 [Fang, 2020](#); [Lawrence et al., 2019](#); [Ross, 1975](#)).

41 At the canopy scale, the probability density of LIA or the fraction of leaf area per unit LIA is expressed as the leaf angle  
42 distribution (LAD) ([De Wit, 1965](#)). [De Wit \(1965\)](#) summarized six theoretical LADs, including planophile, erectophile,  
43 extremophile, plagiophile, uniform, and spherical distributions. Specifically, the spherical distribution assumes that the  
44 relative probability density of the LIA is proportional to the area of the corresponding sphere surface element and its mean  
45 leaf inclination angle (MLA) equals  $57.3^\circ$  ( $MLA = 57.3^\circ$ ) ([De Wit, 1965](#)). Furthermore, [Ross \(1981\)](#) defined the inclination  
46 index ( $\chi_L$ ) to describe the departure of LAD from the spherical distribution. For the planophile distribution,  $\chi_L = 1$ ; for the  
47 erectophile distribution,  $\chi_L = -1$ ; and for the spherical distribution,  $\chi_L = 0$ . In the radiative transfer regime, LIA is generally  
48 represented by the leaf projection function ( $G(\theta)$ ), which is defined as the average projection ratio of unit leaf area in the  
49 illumination or viewing direction  $\theta$  ([Ross, 1981](#); [Nilson, 1971](#)). The spherical distribution is characterized by an isotropic  
50 leaf projection function ( $G \equiv 0.5$ ) ([De Wit, 1965](#)).

51 In the field, LIA can be measured directly based on the leaf's geometrical structure or using indirect optical methods ([Lang,](#)  
52 [1973](#); [Ryu et al., 2010](#); [Norman and Campbell, 1989](#); [Weiss and Baret, 2017](#)). Using these methods, several LIA  
53 measurements have been carried out and some LIA datasets were constructed ([Kattge et al., 2020](#); [Chianucci et al., 2018](#);  
54 [Hinojo-Hinojo and Goulden, 2020](#); [Pisek and Adamson, 2020](#)). These field methods are usually time-consuming and labor-  
55 intensive and are typically difficult to acquire large-scale LIA ([Li et al., 2023](#)). In addition, the existing LIA datasets have  
56 not been comprehensively analyzed. LIA has also been estimated from satellite imagery through empirical relationships or  
57 radiative transfer model inversions ([Zou and Möttus, 2015](#); [Bayat et al., 2018](#); [Goel and Thompson, 1984](#)). Remote sensing  
58 methods are used primarily for crops in local regions, and the generality of these algorithms is limited ([Li et al., 2023](#)). Due  
59 to the difficulty in large-scale LIA measurements and estimations, our knowledge about the global LIA remains lacking.

60 Because our understanding of the global LIA is limited, different LIA simplification strategies have been adopted in various  
61 studies. For example, LIA is typically assumed to follow the spherical distribution ([Tang et al., 2016](#); [Zhao et al., 2020](#);  
62 [Wang and Fang, 2020](#)). However, this assumption may decrease the accuracy of radiative transfer modeling, significantly  
63 underestimate the radiation interception ([Stadt and Liefvers, 2000](#)), and cause large errors ( $>50\%$ ) in leaf area index (LAI)

64 measurements and inversions ([Yan et al., 2021](#)). The spherical LIA assumption may introduce greater error in the nadir  
65 direction than other viewing geometries ([Yan et al., 2021](#)), considering the large G variation in this direction ([Wilson, 1959](#)).  
66 The lack of global LIA knowledge also limits the retrieval of other vegetation structural parameters([Li et al., 2023](#)). In many  
67 LSMs, LIA is commonly treated as a fixed value for different plant function types (PFT) ([Lawrence et al., 2019](#); [Majasalmi](#)  
68 [and Bright, 2019](#)). Field LIA measurements have demonstrated that the spherical distribution is not appropriate for forests,  
69 and the PFT-dependent LIA ignores LIA variation within the PFT ([Pisek et al., 2013](#); [Yan et al., 2021](#); [Majasalmi and Bright,](#)  
70 [2019](#)).

71 This study aims to generate the first global MLA map from existing LIA field measurements using a data-driven gap-filling  
72 method. This method involves spatial expansion and upscaling of LIA measurements, and a random forest regressor using  
73 input spectral, climate, and PFT data. Based on the global MLA map, we tested whether the spherical LIA assumption is  
74 appropriate at the global scale. The new MLA map was validated by comparing the nadir G ( $G(0)$ ) derived from the MLA  
75 with high-resolution reference data. Section 2 outlines the materials and methods employed to generate and evaluate the  
76 global MLA. Section 3 presents the global LIA measurements, global MLA and  $G(0)$ , and evaluation results. Section 4  
77 discusses the performance of the global MLA and  $G(0)$ , the usage of the new MLA map, and the limitations of the study.  
78 Section 5 presents the main conclusions.

## 79 **2 Materials and methods**

### 80 **2.1 LIA measurement data**

#### 81 **2.1.1 TRY LIA dataset**

82 TRY is a network of vegetation scientists headed by Future Earth, the Max Planck Institute for Biogeochemistry, and  
83 German Centre for Integrative Biodiversity Research, providing a global database of curated plant traits (the TRY database)  
84 (<https://www.trydb.org/TryWeb/Home.php>). Since its establishment in 2007, the TRY database has continuously evolved  
85 and has become one of the most widely used vegetation trait databases. The latest V6 version (released on October 13, 2022)  
86 employed in this study contains 15,409,681 trait records covering 305,594 plant taxa ([Kattge et al., 2020](#)). In this database,  
87 LIA was recorded as a numerical or categorical variable. After data extraction and checking, 31,043 valid records were used,  
88 which include numerical LIA, locations, and species. Many measurements lack location information, whereas, for some  
89 locations, there are many measurements for individual species. The spatial distribution map appears relatively sparse despite  
90 a large volume of data (Fig. 1). The LIA measurements in South America are mainly from palms while the LIA  
91 measurements of most species are located in the Northern Hemisphere.

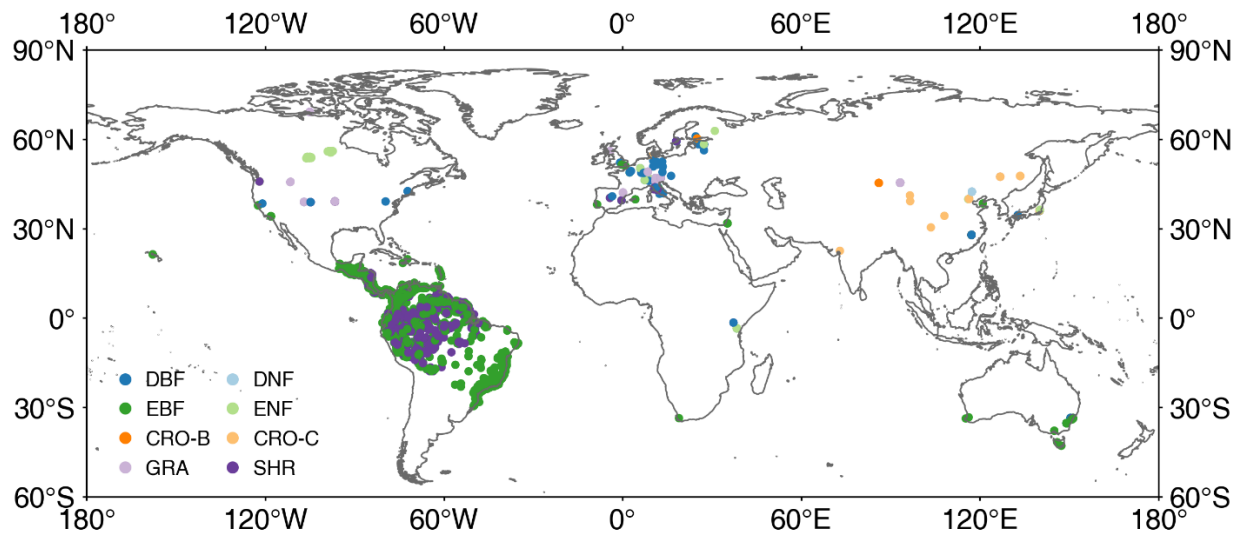


**Figure 1.** The locations of global leaf inclination angle measurements. DBF: deciduous broadleaf forest, DNF: deciduous needleleaf forest, EBF: evergreen broadleaf forest, ENF: evergreen needleleaf forest, CRO-B: broadleaf crops, CRO-C: cereal crops, GRA: grassland, SHR: shrubland.

### 2.1.2 LIA data from the literature

The LIA measurements in published literature were collected via keyword search (leaf angle, leaf inclination angle, and leaf tilt angle) in the Web of Science, Google Scholar, Google, and Chinese documentary databases. The LIA, location, and species information were manually extracted from the literature (Fig. 1). Several LIA measurements were already included in the TRY database (Chianucci et al., 2018; Pisek and Adamson, 2020). After aggregating LIA measurements for the same species at the same location, 780 LIA records were accessed from previous studies (Hinojo-Hinojo and Goulden, 2020; Pisek et al., 2022; Chen et al., 2021).

### 2.1.3 Manual LIA extraction

Only a few measurements in the northern tundra region were obtained, and the measurements in tropical regions are dominated by palm trees (Fig. 1). Therefore, LIA data for the northern tundra and tropical regions were extracted from horizontal side-view photographs searched from Google (Fig. S1). ImageJ software (<https://imagej.nih.gov/ij/>) was used to process the leveled photographs and derive LIA following the method of Pisek et al. (2011). The TRY species location data (848,919, Fig. S3b) (Jan 03, 2022) were used to obtain the dominant species information in tropical rainforests and the northern tundra. The species location points in these two vegetation types were spatially filtered and the frequency of occurrence for each species was counted. The species with a high frequency of occurrence were selected to measure the LIA. For each species, more than 75 leaves perpendicular to the viewing direction were selected and processed based on visual

112 judgment to ensure the stability and reliability of the MLA ([Pisek et al., 2013](#)). In total, the MLA of 104 species was  
113 manually derived.

114 In this study, most LIA measurements are obtained with protractor and level digital photogrammetry, especially for  
115 needleleaf species. Therefore, the distinction between branches and leaves is considered. The diverse LIA records from  
116 different sources were sorted to match the TRY species and to get the PFT based on the TRY Categorical Traits Dataset  
117 2018 (<https://www.try-db.org/TryWeb/Data.php#3>). LIA measurements from different sources were unified into canopy-  
118 level MLA with average operation by leaf number (see Appendix A). If there were multiple LIA records for the same species,  
119 the mean value was computed for the same location and species. In total, 5,554 LIA records of 1,194 species were collected,  
120 covering the growing season from 2001 to 2022. LIA location replicates per species range from 1 to 330, and most replicates  
121 (98 %) are less than 50. Considering the different numbers of records for each species, the LIA data was further aggregated  
122 by species.

## 123 **2.2 Remote sensing data**

### 124 **2.2.1 Ancillary data used for MLA mapping**

125 The ancillary data used for global MLA mapping and analysis are listed in Table 1. Most earth observation data were  
126 accessed and processed in Google Earth Engine (GEE) (<https://earthengine.google.com/>). The PFT classification system in  
127 the MODIS global 500 m land cover type product (MCD12Q1 C6) was used and mode-aggregated from 2001 to 2022 to  
128 match the LIA measurements (Fig. S2) ([Sulla-Menashe et al., 2019](#)). The 2001–2022 Landsat surface reflectance (Level 2,  
129 Collection 2, Tier 1) ([Crawford et al., 2023](#)), including Landsat 5 (2001–2012), Landsat 7 (2012–2013), and Landsat 8  
130 (2013–2022) was utilized to generate a global 30 m PFT map (Section 2.3.1), which was subsequently employed for LIA  
131 upscaling. Considering the sensitivity of directional reflectance variation to LIA ([Jacquemoud et al., 2009](#); [Li et al., 2023](#)),  
132 the 2001–2022 MODIS bidirectional reflectance distribution function (BRDF) model parameters dataset (MCD43A1 C6.1)  
133 ([Schaaf and Wang, 2015b](#)) and nadir BRDF adjusted reflectance dataset (MCD43A4 V6 NBAR) ([Schaaf and Wang, 2015a](#))  
134 produced daily using 16 days of Terra and Aqua MODIS data at 500 m resolution and were utilized as predictive variables.  
135 We used MCD43A1 C6.1 and MCD12Q1 and MCD43A4 C6 for MLA mapping as these data were available on GEE when  
136 this study was conducted. Only minor calibration changes and polarization correction were adopted in the upgrading from  
137 Collection 6 to 6.1, while the MCD12Q1 and MCD43A4 algorithms remain the same  
138 ([https://landweb.modaps.eosdis.nasa.gov/data/userguide/MODIS\\_Land\\_C61\\_Changes.pdf](https://landweb.modaps.eosdis.nasa.gov/data/userguide/MODIS_Land_C61_Changes.pdf)). In addition, the multi-year  
139 aggregation of these products (Table 2) further mitigates the version impact. Due to the scarcity of crop LIAs and the lack of  
140 location information for existing crop LIA measurements, fine-resolution (10/30 m) crop-type maps (Table 1) in 2018 were  
141 employed to support crop LIA mapping. Other data include the ERA5-Land reanalysis data, the ALOS digital elevation  
142 model (AW3D30 V3.2), and the 2001–2022 MODIS LAI product (MCD15A2H) ([Myneni, 2015](#)). The LAI product was  
143 averaged and aggregated from 2001–2022.

144

145 **Table 1.** Remote sensing data for global MLA mapping. BRDF: bidirectional reflectance distribution function.

Category	Data	Year	Spatial resolution	Temporal resolution	Reference
Plant function type	MCD12Q1 C6	2001–2022	500 m	Yearly	( <a href="#">Sulla-Menashe et al., 2019</a> )
Surface reflectance	Landsat collection 2	2001–2022	30 m	16 days	( <a href="#">Crawford et al., 2023</a> )
	MCD43A4 V6 NBAR	2001–2022	500 m	Daily	( <a href="#">Schaaf and Wang, 2015a</a> )
BRDF	MCD43A1 C6.1	2001–2022	500 m	Daily	( <a href="#">Schaaf and Wang, 2015b</a> )
Crop type	Cropland Data Layers (CDL)	2018	30 m	Yearly	( <a href="#">Boryan et al., 2011</a> )
	EUCROPMAP	2018	10 m	Yearly	( <a href="#">D’andrimont et al., 2021</a> )
	AAFC Annual Crop Inventory	2018	30 m	Yearly	( <a href="#">Fisette et al., 2013</a> )
	Northeast China crop-type map	2018	30 m	Yearly	( <a href="#">You et al., 2021</a> )
	NESEA-Rice10	2018	10 m	Yearly	( <a href="#">Han et al., 2021</a> )
	China maize map	2018	30 m	Yearly	( <a href="#">Shen et al., 2022</a> )
	China winter wheat map	2018	30 m	Yearly	( <a href="#">Dong et al., 2020</a> )
Climate	ERA5-Land	2001–2022	0.1°	Monthly	( <a href="#">Muñoz-Sabater et al., 2021</a> )
Terrain	AW3D30 V3.2	—	30 m	—	( <a href="#">Tadono et al., 2014</a> )

146 **2.2.2 High-resolution reference data**

147 The high-resolution reference datasets provided by Ground Based Observations for Validation (GBOV,  
148 <https://land.copernicus.eu/global/gbov/dataaccessLP/>) and DIRECT 2.1 (<https://calvalportal.ceos.org/lpv-direct-v2.1>) were  
149 used to evaluate the generated global MLA (Fig. 2). These datasets provide high-resolution (20/30 m) LAI, effective LAI  
150 (LAIe), and fractional vegetation cover (FVC) data over a 3 km × 3 km area centered on each site generated using empirical  
151 relationships between various vegetation indices and ground measurements ([Li et al., 2022](#); [Brown et al., 2020](#)). GBOV has  
152 provided continuous high-resolution reference data since 2013 (Fig. 2).

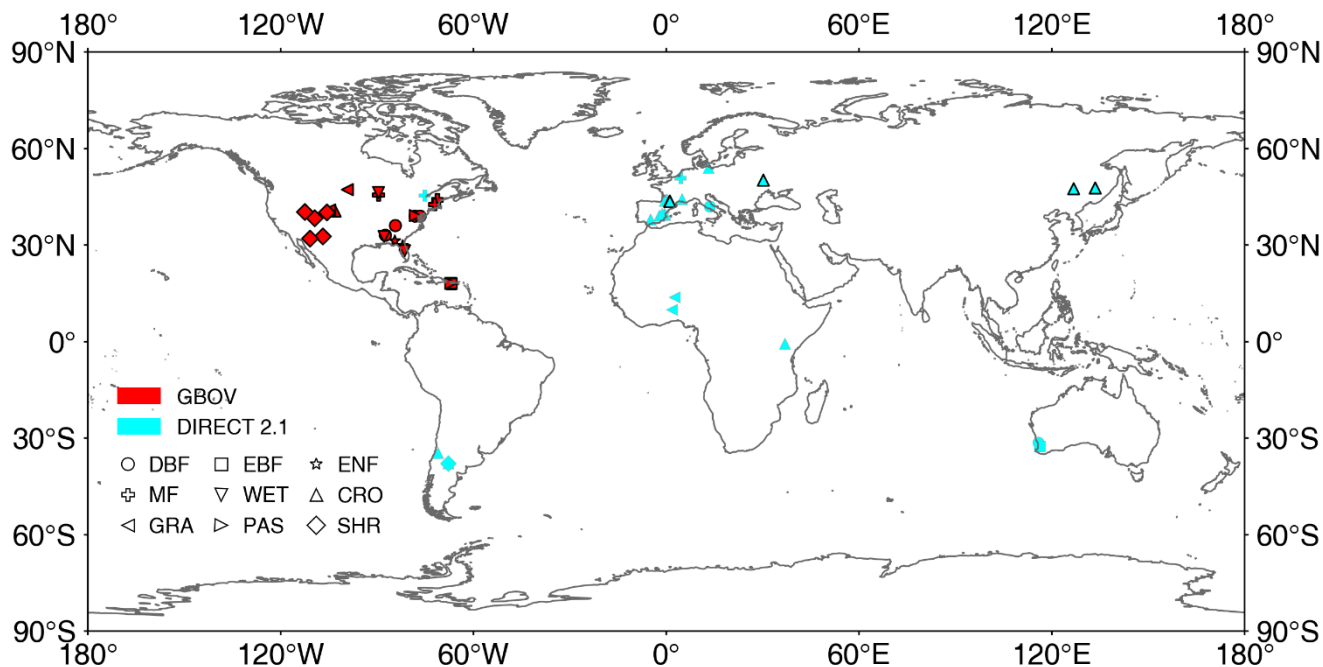


**Figure 2.** Locations of GBOV and DIRECT 2.1 sites used in this study. CRO: Cultivated crops, MF: Mixed forest, PAS: Pasture/hay, WET: Woody wetlands. See Fig. 1 for other acronyms. The black frame indicates those sites with >5 continuous records.

## 2.3 Mapping global LIA

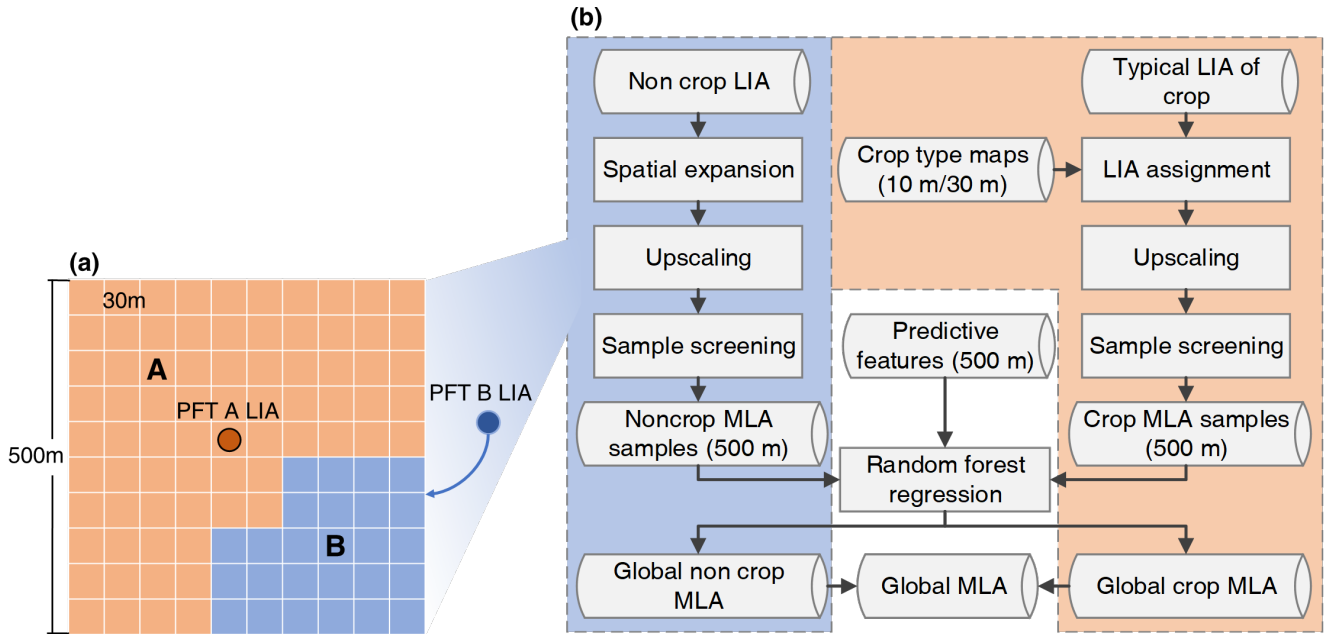
### 2.3.1 Data preparation

Many studies have treated LIA as a species-specific static trait and ignored within-species variations when LIA measurements are limited (Pisek et al., 2022; Toda et al., 2022; Raabe et al., 2015). Following the rationale, the spatial coverage of LIA measurements was expanded, and those records without location information were utilized (section 2.1.1). Under this assumption, the LIA measurements were expanded through TRY species location data with species name matching. The species location data comprises trait measurements for common species representing a hundreds-of-square-meter area around the location. The dominant species was artificially identified by investigators and thus the spatial representativeness is considered. When a species had multiple LIA observations at different locations, the nearest LIA was assigned to the TRY species location. Visual inspections were conducted to remove potential TRY location biases, especially for non-vegetated points such as water bodies and deserts. After spatial expansion, the number of LIAs reached 12,328 and its spatial distribution became more uniform (Fig. S3c).

In this study, the scale gap between field measurements and satellite remote sensing data was fully considered. The canopy level MLA measurement is regarded as equal to 30 m-MLA considering its spatial representativeness. To upscale the MLA measurements from canopy level to the satellite resolution (500 m), a 30 m PFT map was first derived from Landsat

171 reflectance using a random forest classification method. The random forest was trained at a 500 m scale using the mode-  
 172 aggregated MODIS PFT classification map as training samples to generate a 30 m PFT map by hierarchically selecting  
 173 homogeneous pixels (with a coefficient of variation in reflectance < 0.2). The classification features were the same as those  
 174 in the MODIS classification algorithm (Sulla-Menashe et al., 2019). For a 500 m pixel with multiple PFTs (Fig. 3a), when  
 175 one PFT had no MLA measurement, the MLA of the PFT was assigned with the value of its nearest neighbor within 100 km  
 176 with the same PFT. This distance setting (100 km) was based on a previous study that derived global maps for various leaf  
 177 traits from a limited number of field measurements, remote sensing, and climate data (Moreno-Martínez et al., 2018). In field  
 178 measurement, the entire canopy MLA is commonly calculated as the average of all measured leaf LIAs weighted by leaf area  
 179 (see Appendix A) (Zou et al., 2014; De Wit, 1965; Yan et al., 2021). Leaves with larger areas have higher weights.  
 180 Upscaling MLA from 30 m to 500 m follows the same rationale as that from leaf to canopy scale. For a 30 m pixel with a  
 181 higher LAI, the weight of the pixel is higher. Therefore, the 500 m MLA was computed as the weighted average of the  
 182 enhanced vegetation index (EVI2) assuming a linear relationship between LAI and EVI2 (see Appendix A) (Dong et al.,  
 183 2019; Alexandridis et al., 2019). Although previous studies have reported that vegetation index may be nonlinearly  
 184 correlated to LAI because of the saturation effect at medium and high LAI conditions, EVI2 is highly resistant to the  
 185 saturation effect (Gao et al., 2023). The errors caused by this slight nonlinearity were further analyzed in Section 4.4.

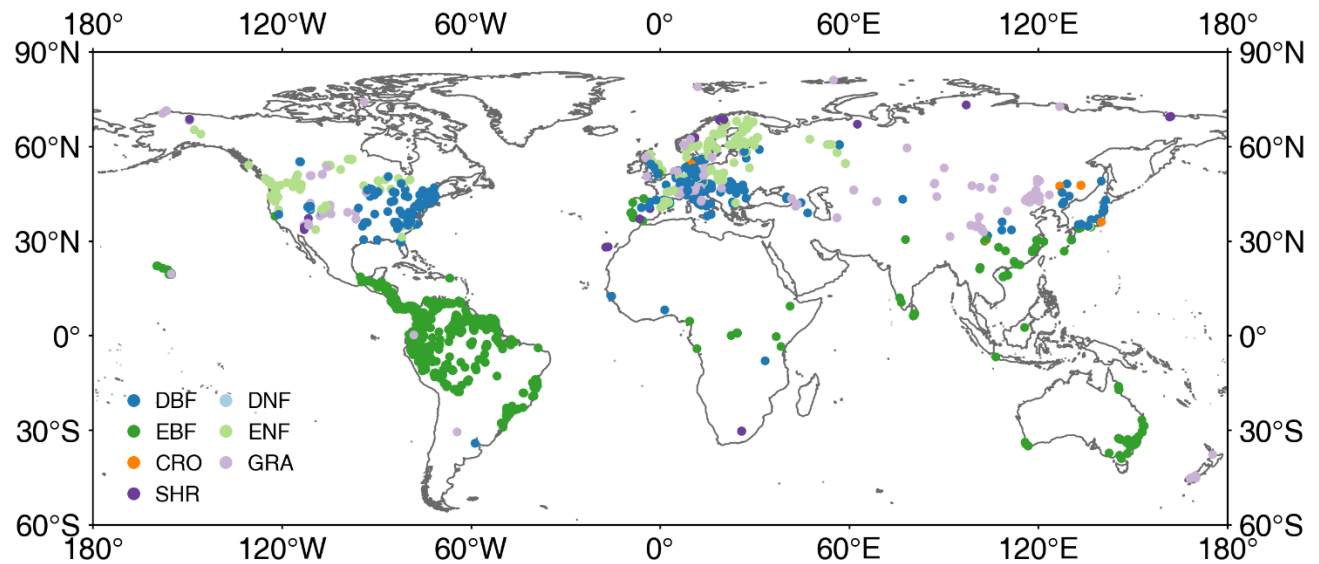
186 
$$MLA_{500m} = \frac{\sum MLA_{30m} \times EVI2_{30m}}{\sum EVI2_{30m}} \quad (1)$$



187  
 188 **Figure 3.** Leaf inclination angle (LIA) upscaling (a) and global mean LIA (MLA) mapping (b) strategies.



189 The 500 m upscaled MLA samples were further refined to select the most representative samples following three criteria: 1)  
 190 the coefficient of variation of the 30 m EVI2 in the 500 m pixel is less than 0.2, 2) the vegetation proportion in the 500 m  
 191 pixel is greater than 0.8, and 3) the proportion of PFTs represented by the MLA measurements in the 500 m pixel is greater  
 192 than 0.4. The final number of samples after refinement is 3,013 with a uniform spatial distribution (Fig. 4).



193  
 194 **Figure 4.** Distribution of global mean leaf inclination angle samples after screening. See Fig. 1 for acronyms.

### 195 2.3.2 Global MLA mapping

196 Different mapping strategies were employed for noncrops and crops (Fig. 3b) considering the small number of valid crop  
 197 samples (Fig. 4) and the lack of location information for most crop samples. For noncrops, the upscaled 500 m MLA  
 198 samples were used to train a random forest regressor to predict the global MLA from different features (Table 2). All input  
 199 features were unified to the 500 m resolution. Therefore, the derived MLA map corresponds to the average MLA at the 500  
 200 m scale. Notably, this study used all MODIS BRDF and spectral reflectance data including low-quality ones that may be  
 201 contaminated by clouds. The multi-year aggregation (Table 2) can partly mitigate the influence induced by low-quality  
 202 observations ([Sulla-Menashe et al., 2019](#)). Normalized difference vegetation index (NDVI) was used as the predictive  
 203 feature because it is strongly coupled with LIA, especially under low and medium vegetation density conditions ([Dong et al.,](#)  
 204 [2019](#); [Zou and Möttus, 2015](#)). To reduce computational complexity and potential overfitting, a feature selection process was  
 205 conducted based on the variable importance (the sum of the decrease in Gini impurity index over all trees in the forest)  
 206 computed by the model, and only the 40 most important variables were used in the final prediction. During the training  
 207 process, the out-of-bag error was minimized to obtain the optimal hyperparameters. The prediction performance of the  
 208 random forest regressor was evaluated using a ten-fold cross-validation approach with upscaled MLA samples.

For crops, the measured MLA values were averaged for different crop types as a typical MLA (Table S2). After assigning typical MLAs for different crops with high-resolution crop maps (Table 1), the high-resolution crop MLA were upscaled to 500 m as training samples (Eq. (1)). Only the samples with a crop area ratio > 80% within a 500 m pixel were selected for training. The crops were further divided into broadleaf crops and cereal crops and processed with the same procedure used for noncrops (Fig. 3b). All procedures were conducted on GEE under the WGS-84 geographic coordinate system. Two quality layers were added to represent the quality of input data and the prediction model. The input data quality was denoted by the proportion of high-quality BRDF inversions for each pixel. The prediction model quality was represented qualitatively for each pixel considering whether the MLA was predicted by extrapolating beyond the range of the training samples. The random forest model is typically regarded as a black-box and its uncertainty is difficult to quantify in the present study.

**Table 2.** Predictive features in global MLA mapping.

Category	Features	Variables	Number
Spectral	Blue, green, red, near-infrared reflectance	10%, 33%, 50%, 67%, 90% quantiles and standard deviation	24
	NDVI	10%, 33%, 50%, 67%, 90% quantiles and standard deviation	6
BRDF	Kernel coefficients of the red band	10%, 33%, 50%, 67%, 90% quantiles and standard deviation	18
	Kernel coefficients of near-infrared band	10%, 33%, 50%, 67%, 90% quantiles and standard deviation	18
PFT	PFT	Constant	1
Climate	Solar downward radiation	Mean and standard deviation	2
	Temperature	Mean and standard deviation	2
	Precipitation	Mean and standard deviation	2
Terrain	Elevation	Constant	1
	Slope	Constant	1
	Aspect	Constant	1

**2.4 Evaluation of global MLA**

The global MLA map was indirectly evaluated using the nadir leaf projection function, because of the lack of high-resolution reference MLA.  $G(0)$  is important because it is coherent with the satellite nadir observations. The global  $G(0)$  was derived from the MLA and evaluated with high-resolution reference following the upscaling scheme recommended by the Land Product Validation (LPV) Subgroup of the Committee on Earth Observation Satellites (CEOS) (<http://lpvs.gsfc.nasa.gov/>). Assuming a single-parameter ellipsoidal leaf angle distribution ([Campbell, 1990](#); [Wang et al., 2007](#)), the parameter  $\chi$ , the ratio of the horizontal and vertical axes of an ellipsoid, was first derived from MLA in radians. Compared to other models, the single-parameter ellipsoidal leaf angle distribution is a relatively more accurate and simpler model and has been used in many remote sensing studies ([Campbell, 1990](#); [Wang et al., 2007](#); [Kuusk, 2001](#); [Verhoef et al., 2007](#)).

$$\chi = -3 + \left(\frac{MLA}{9.65}\right)^{-0.6061} \quad (2)$$

The  $G(\theta)$  value in the nadir direction ( $\theta=0^\circ$ ) was calculated using the following analytical formula.

$$G(\theta) = \frac{\sqrt{(\chi^2 + \tan^2 \theta) \cos \theta}}{\chi + 1.774(\chi + 1.182)^{-0.73}} \quad (3)$$

The reference  $G(0)$  was derived from high-resolution LAI, FVC, and clumping index (CI) ( $=LAI_e/LAI$ ) with the Beer-Lambert law (Fig. S4) (Nilson, 1971).

$$P(\theta) = \exp \left( -\frac{G(\theta) * LAI * CI(\theta)}{\cos(\theta)} \right) \quad (4)$$

Where  $P(\theta)$ ,  $CI(\theta)$ , and  $G(\theta)$  denote the gap fraction, CI, and  $G$  in direction  $\theta$ , respectively. Specifically, the gap fraction in the nadir direction can be expressed by FVC.

$$P(0) = 1 - FVC \quad (5)$$

Therefore, the reference  $G(0)$  was derived using the following formula.

$$G(0)_{CI(0)} = -\frac{\ln(1-FVC)}{CI(0) * LAI} \quad (6)$$

By using the whole CI as the nadir CI ( $CI(0)$ ) in the above equation (Fang et al., 2021; Li et al., 2022),  $G(0)$  was calculated as follows:

$$G(0)_{CI} \approx -\frac{\ln(1-FVC)}{CI * LAI} \quad (7)$$

The MLA product was first upscaled to 3 km through a weighted averaging method using the MODIS LAI to derive  $G(0)$  (Eq. (3)). The reference LAI, FVC, and CI were also upscaled to 3 km through simple averaging to compute the reference  $G(0)$  (Eq. (7)). The MLA-derived  $G(0)$  and the reference  $G(0)$  were compared at the  $3 \text{ km} \times 3 \text{ km}$  area around each site. The correlation coefficient ( $r$ ), bias, and root mean square error (RMSE) were calculated as the evaluation metrics, as follows:

$$r = \sqrt{1 - \frac{\sum_{i=1}^n (\hat{y}_i - y_i)^2}{\sum_{i=1}^n (y_i - \bar{y})^2}} \quad (8)$$

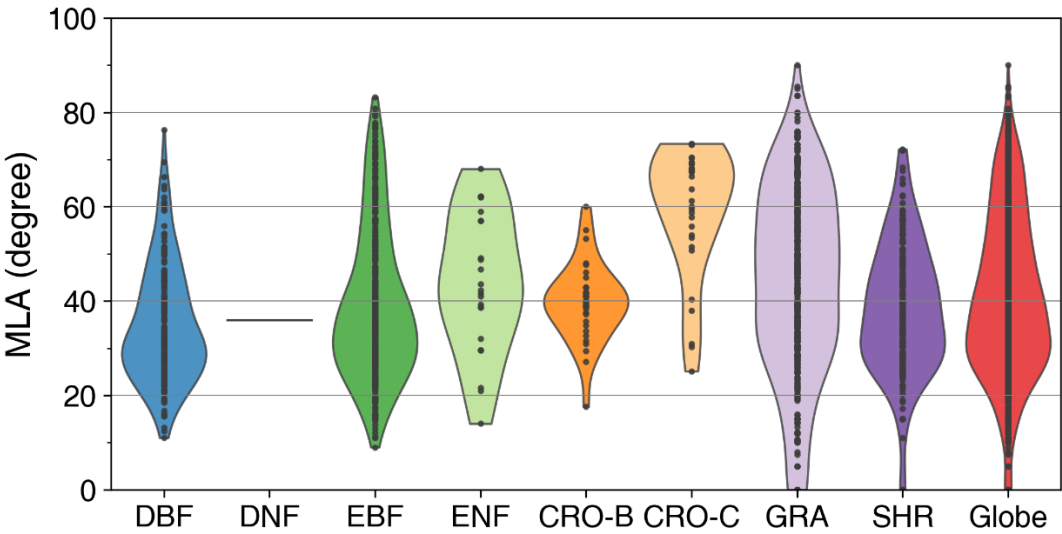
$$Bias = \frac{1}{n} \sum_{i=1}^n (\hat{y} - y_i) \quad (9)$$

$$RMSE = \sqrt{\frac{1}{n} \sum_{i=1}^n (\hat{y} - y_i)^2} \quad (10)$$

where  $\hat{y}_i$ ,  $y_i$ , and  $n$  denote the MLA-derived  $G(0)$ , reference  $G(0)$ , and the number of  $G(0)$ , respectively.

253 **3.1 Global measured LIA values**

254 The species-aggregated LIA was employed in the analysis of global LIA measurements. Fig. 5 shows the distributions of  
255 global measured LIA values for different PFTs. The global measured MLA is 40.74° and generally follows the order of  
256 CRO-C > GRA > ENF > CRO-B > EBF > SHR > DNF > DBF (Table 3). Cereal crops exhibit the highest MLA (59.11°),  
257 whereas DBF has the most horizontal leaves (MLA = 34.94°). GRA and EBF show large LIA variations (Std = 20.44° and  
258 17.17°), whereas CRO-B exhibits a small range. The DNF LIA measurements are only for one species and show very little  
259 variation (Fig. 5).



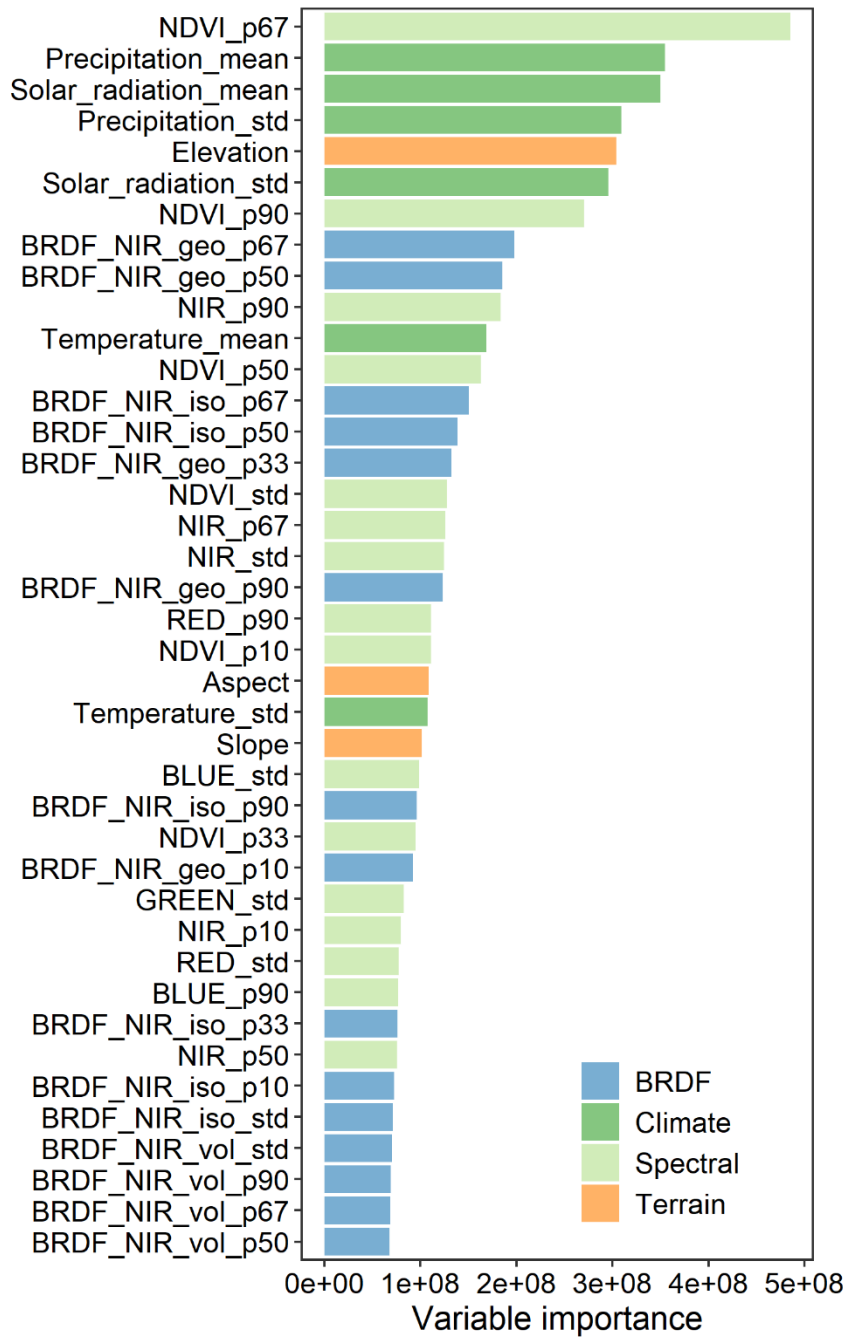
260  
261 **Figure 5.** Distribution of global mean LIA (MLA) for different plant function types (see Fig. 1 for acronyms). The last shape shows the  
262 global average. Statistics are conducted for each species as represented by points in the figure.

263  
264 **Table 3.** Statistics of leaf inclination angle measured for different plant functional types (PFT). STD is the standard deviation. The  
265 inclination index ( $\chi_L$ ) is converted from mean leaf inclination angle (MLA) ( $\chi_L = 2\cos(\text{MLA}) - 1$ ) (Lawrence et al., 2019).

PFT	DBF	DNF	EBF	ENF	CRO-B	CRO-C	GRA	SHR	Globe
Number of species	171	1	347	23	32	31	399	190	1194
Mean(°)	<b>34.94</b>	35.88	39.30	43.69	39.71	<b>59.11</b>	44.13	38.32	40.74
STD (°)	12.40	0.00	<b>16.11</b>	14.40	8.11	13.28	<b>20.17</b>	13.80	17.12
$\chi_L$	0.64	0.62	0.55	0.45	0.54	0.03	0.44	0.57	0.52

266 **3.2 The relationships between MLA and other variables**

267 Fig. 6 shows the importance of the top 40 variables in the MLA prediction obtained from the random forest regression model.  
268 The importance of these 40 variables accounts for 78% of the total importance among all 76 variables. Spectral features  
269 account for 30% of the importance, which is higher than that of other features. Among the spectral features, NDVI, near-  
270 infrared (NIR) band, and red band reflectance are most critical for MLA prediction. The importance of BRDF features is  
271 comparable to that of climatic variables (21% vs. 20%), followed by terrain features (7%). Among the BRDF features, the  
272 NIR BRDF information shows a higher contribution than the red band, with importance in the following order: geometrically  
273 scattered kernel> isotropic scattering kernel > volumetric scattering kernel. The importance ranking of the climatic variables  
274 follows the order of precipitation  $\approx$  solar radiation > temperature. In addition, elevation, slope, and aspect significantly  
275 impact on the MLA prediction.



276

277 **Figure 6.** The importance of variables in the mean leaf inclination angle prediction. NIR, Red, Green, and Blue denote the nadir  
 278 reflectance in near-infrared, red, green, and blue bands, respectively; geo, iso, and vol represent kernel coefficients of geometric-optical  
 279 surface scattering, isotropic scattering, and volumetric scattering, respectively. The suffixes p××, mean, and std represent ××% quantile,  
 280 mean, and standard deviation, respectively.

Fig. 7 illustrates the relationships between the upscaled MLA samples and the 16 most important variables. Overall, MLA decreases with the increase of NDVI, NIR reflectance, and NIR BRDF kernel parameters, whereas it increases with the standard deviation of NDVI. MLA is negatively correlated with solar radiation, precipitation, and temperature. Additionally, MLA increases with increasing the standard deviation of solar radiation (corresponding to mid-to-high latitude regions), while it decreases with the increase in the standard deviation of precipitation (corresponding to tropical and subtropical regions with high precipitation). MLA increases slightly with altitude and then decreases.

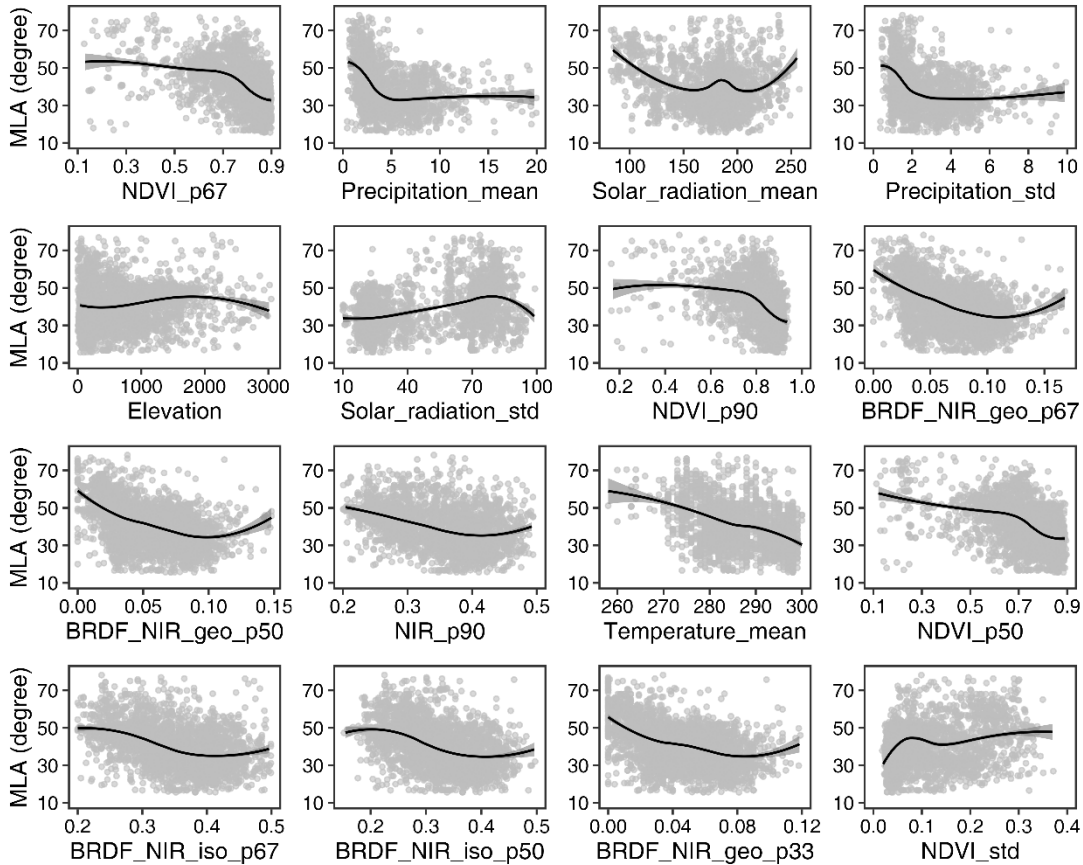
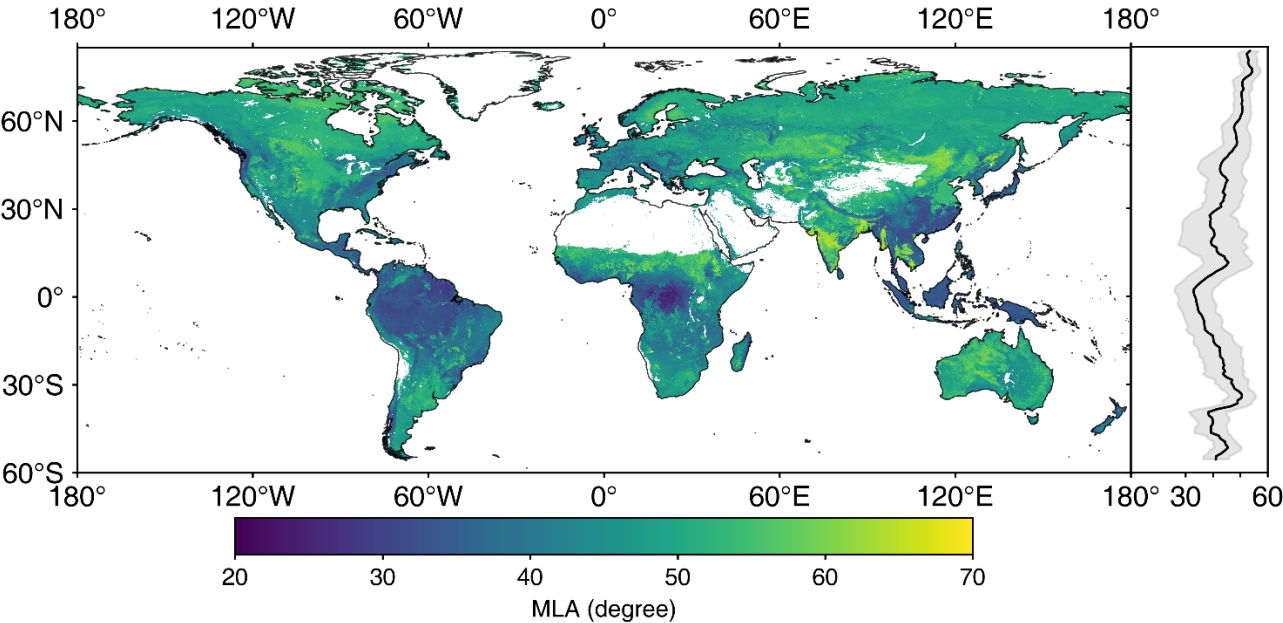


**Figure 7.** Relationships between mean leaf inclination angle (MLA) and different predictive variables. See Fig. 6 for different variables.

### 3.3 Global MLA and G(0) maps

Fig. 8 shows the spatial distribution of the global 500 m MLA product. Central Asia (grasslands), southern India (cereal crops), and the central United States (grasslands and cereal crops) show higher MLAs of approximately 60°, whereas the rainforests and Southeast Asia forests have more horizontal leaves with MLAs of around 30° (Fig. 8 and S2). MLA increases with latitude, from  $32.93 \pm 7.03^\circ$  around the equator ( $\sim 1.5^\circ$  N) to  $53.48 \pm 3.20^\circ$  in the northern tundra ( $\sim 76.5^\circ$  N). Variation in MLA decreases as latitude increases (Fig. 8). Among different PFTs, cereal crops show the highest MLA ( $54.65 \pm 6.28^\circ$ ),

295 while evergreen broadleaf forest has the lowest MLA ( $34.40 \pm 6.42^\circ$ ), and PFTs follow the order: CRO-C > CRO-B > DNF >  
 296 SHR > ENF  $\approx$  GRA > DBF > EBF (Table 4). Grassland, broadleaf forest, and evergreen needleleaf forests show larger MLA  
 297 variations than other PFTs, whereas deciduous needleleaf forests show minimal variation. The global vegetation MLA is  
 298  $41.47^\circ$ , with a standard deviation of  $9.55^\circ$ , which is comparable to the MLA of DBF ( $41.23 \pm 6.58^\circ$ ) (Fig. 9a and Table 4).



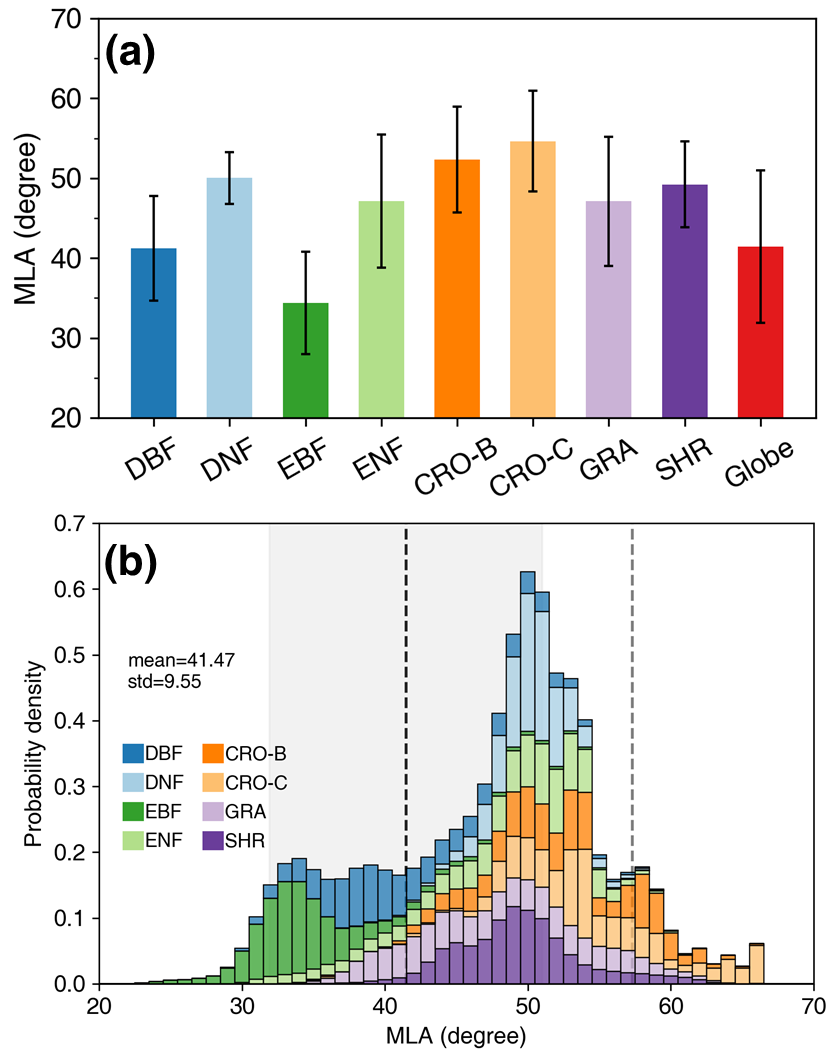
299  
 300 **Figure 8.** The global mean leaf inclination angle (MLA) map. The right panel shows the MLA latitudinal mean (solid line) and the  
 301 standard deviation values (shaded area) weighted by leaf area index.

302 **Table 4.** Statistics of global mean leaf inclination angle (MLA), nadir leaf projection function ( $G(0)$ ), and inclination index ( $\chi_L$ ) for  
 303 different plant functional types (PFT). STD is the standard deviation. The  $\chi_L$  is converted from MLA ( $\chi_L = 2\cos(\text{MLA}) - 1$ ) ([Lawrence](#)  
 304 [et al., 2019](#)).

PFT	DBF	DNF	EBF	ENF	CRO-B	CRO-C	GRA	SHR	Globe
Area proportion(%)	14.02	6.32	15.08	11.42	2.99	6.84	28.45	14.88	100.00
MLA( $^\circ$ )	41.23	50.05	<b>34.40</b>	47.13	52.35	<b>54.65</b>	47.12	49.23	41.47
STD of MLA ( $^\circ$ )	6.58	3.24	6.42	8.35	6.63	6.28	8.08	5.35	9.55
$G(0)$	0.69	0.58	<b>0.76</b>	0.61	0.55	<b>0.52</b>	0.61	0.59	0.68
STD of $G(0)$	0.07	0.03	0.06	0.08	0.07	0.08	0.09	0.06	0.11
$\chi_L$	0.50	0.28	0.65	0.36	0.22	0.16	0.36	0.31	0.50

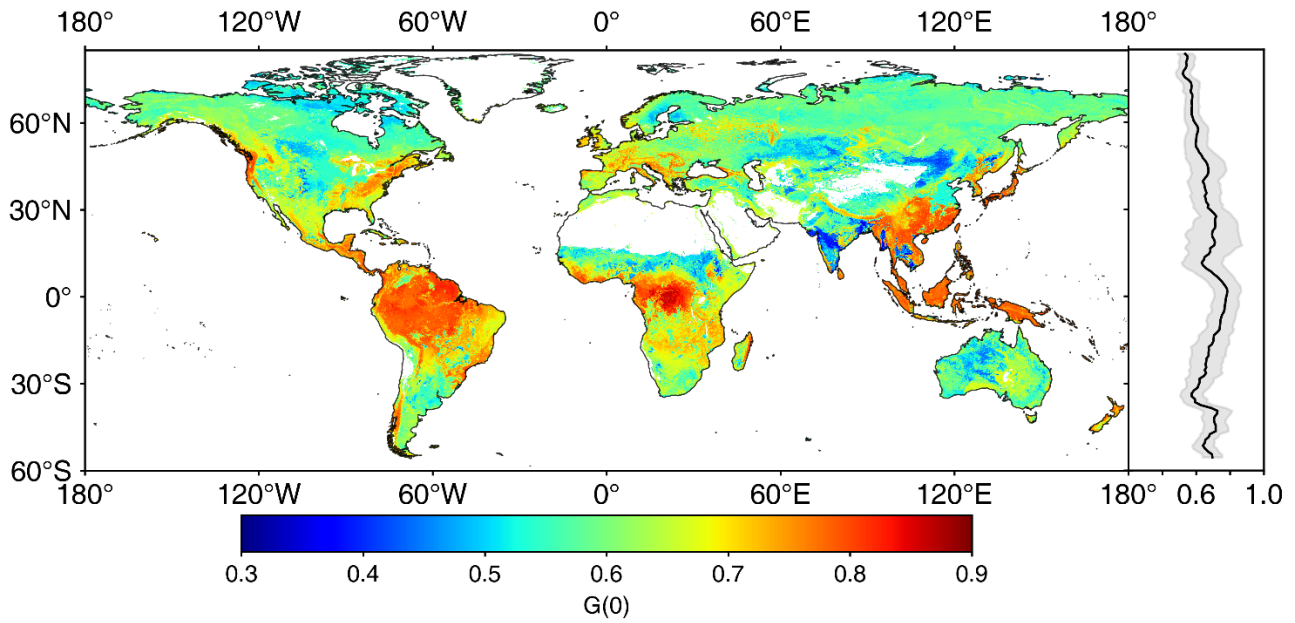
305  
 306 The global MLA exhibits an asymmetric probability density distribution toward the lower MLA (Fig. 9b). It roughly  
 307 presents three peaks, with the highest peak ( $\sim 51^\circ$ ) containing DNF, ENF, CRO, GRA, and SHR. The moderate peak ( $\sim 35^\circ$ )  
 308 is mainly composed of EBF and DBF, while the third peak ( $\sim 58^\circ$ ) is dominated by crops. The MLAs of crops and some  
 309 grasslands are close to the MLA of the spherical distribution ( $57.30^\circ$ ). The global MLA ( $41.47^\circ$ ) is  $15.83^\circ$  (38%) smaller  
 310 than the MLA of the spherical distribution because the vegetation MLA is mostly less than  $57.30^\circ$  (Fig. 9b).





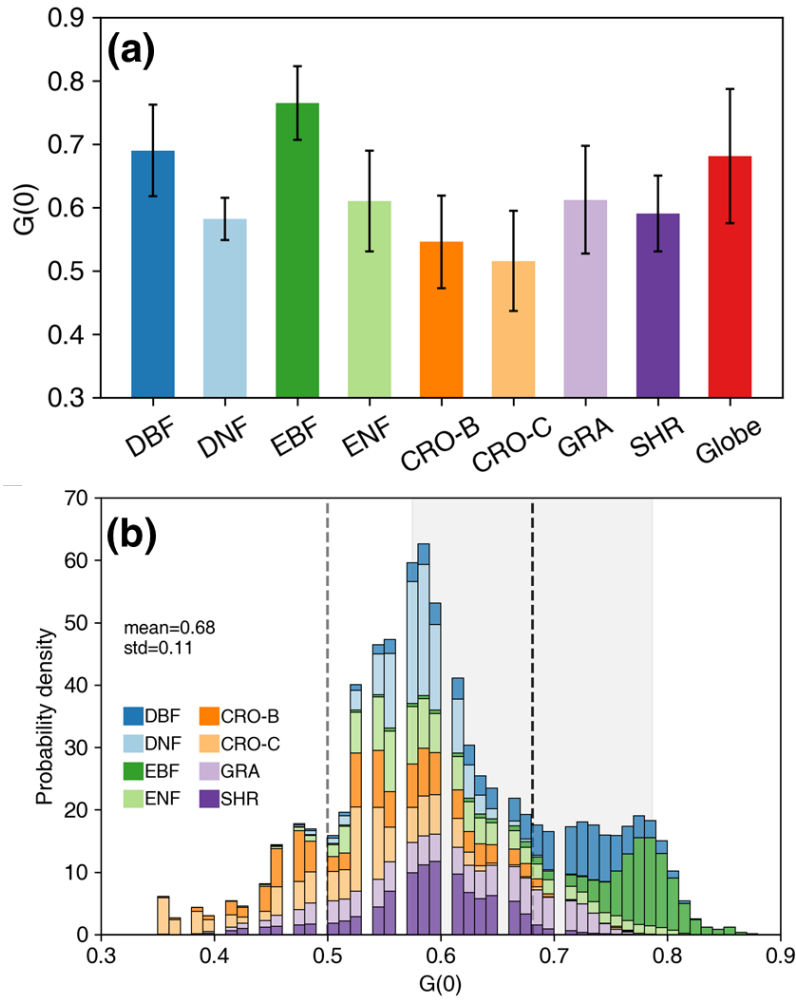
311  
 312 **Figure 9.** Statistics (a) and probability density distributions (b) of the global mean leaf inclination angle (MLA) for different plant  
 313 functional types. The error bars in (a) represent the standard deviation. The black dash line and shade area in (b) indicate the global MLA  
 314 mean and standard deviation. The gray dashed line represents the MLA ( $=57.30^\circ$ ) of spherical leaf angle distribution. The mean, standard  
 315 deviation, and probability density values are weighted by leaf area index. See Fig. 1 for the acronyms.

316 Fig. 10 displays the spatial distribution of global  $G(0)$  generated from MLA. Overall, the global  $G(0)$  shows an opposite  
 317 pattern with the global MLA. The  $G(0)$  values in Central Asia (grasslands, Fig. S2), southern India (cereal crops), and the  
 318 central United States (grasslands and cereal crops) are relatively lower than those in tropical rainforests, forests in Southeast  
 319 Asia, and forests in the eastern United States.  $G(0)$  generally decreases slowly with latitude, from  $0.78 \pm 0.08$  at the equator  
 320 ( $\sim 1.5^\circ$  N) to  $0.52 \pm 0.04$  in the northern tundra ( $\sim 76.5^\circ$  N).



321  
 322 **Figure 10.** The global nadir leaf projection function ( $G(0)$ ) map. The right panel shows the  $G(0)$  mean (solid line) and standard deviation  
 323 values (shaded area) weighted by leaf area index.

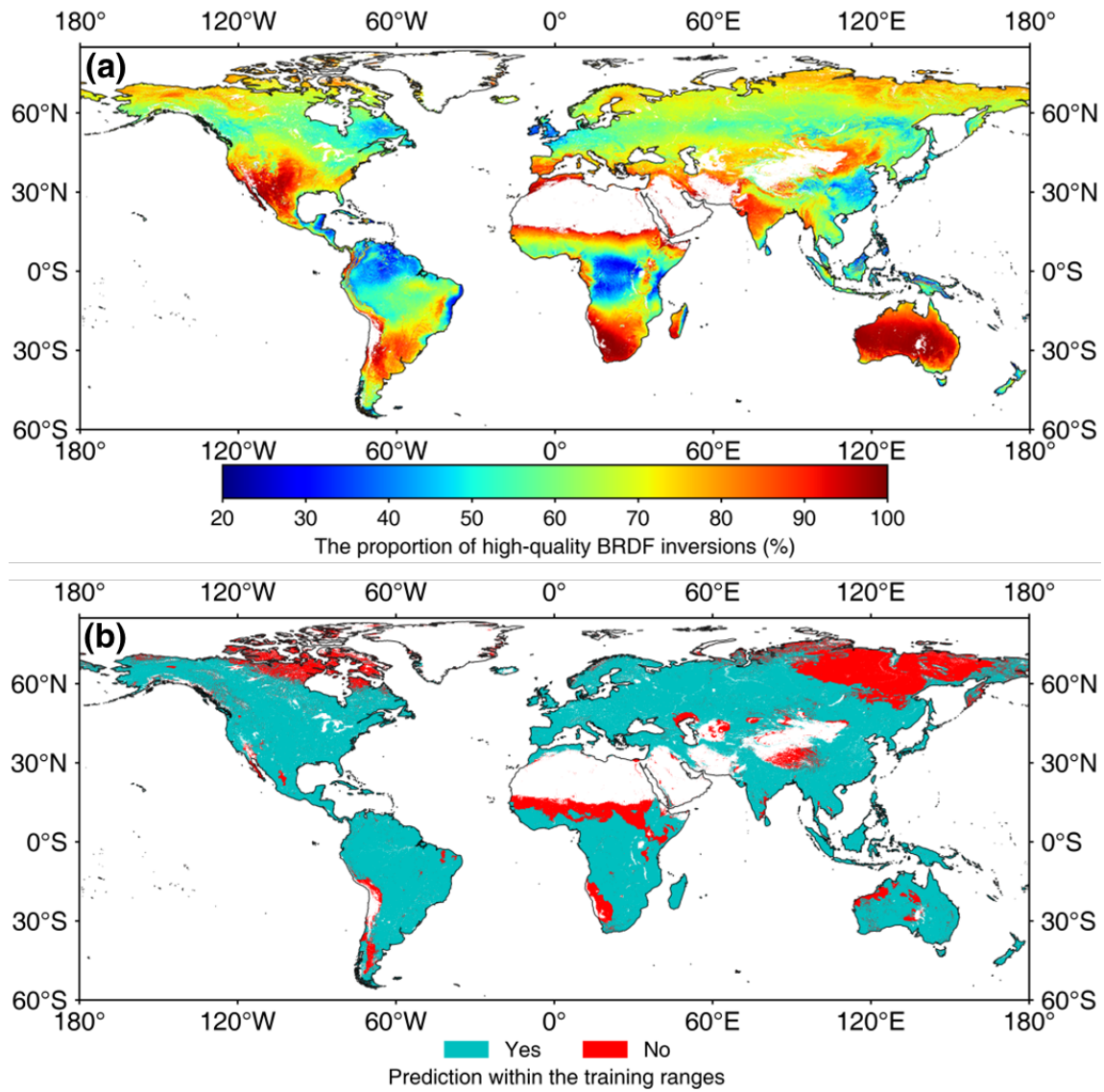
324 Among different PFTs, EBF has the highest  $G(0)$ , at approximately  $0.76 \pm 0.06$  (Fig. 11a, Table 4), whereas cereal crops  
 325 show the lowest value, at approximately  $0.52 \pm 0.08$ . The DBF  $G(0)$  is comparable to the global average. The  $G(0)$  of broad-  
 326 leaved forests is greater than that of other PFTs (Fig. 11a, Table 4). The global  $G(0)$  probability density distribution peaks at  
 327 0.52–0.65, with an asymmetric distribution (Fig. 11b). The proportion on the right side of the peak is larger than that on the  
 328 left. The peak of the global  $G(0)$  distribution mainly contains DNF, ENF, CRO, GRA, and SHR. The left side of the peak is  
 329 mainly composed of crops, while the right side is dominated by broad-leaved forests and some shrubs. The spherical  
 330 distribution  $G(0)$  (0.50) is mainly represented by crops and a small amount of grassland, where  $G(0)$  also shows a large  
 331 variation ( $\sim 0.35$ ). The spherical distribution  $G(0)$  is 0.18 (26%) less than the global average  $G(0)$  (0.68), as most vegetation  
 332  $G(0)$  is greater than 0.50 (Fig. 11b).



333

334 **Figure 11.** Statistics (a) and probability density distributions (b) of the global nadir leaf projection function ( $G(0)$ ) for different plant  
335 functional types. The error bars in (a) represent the standard deviation. The black dash line and shade area in (b) indicate the global  $G(0)$   
336 mean and standard deviation. The gray dashed line represents the  $G(0)$  ( $=0.50$ ) of spherical leaf angle distribution. The mean, standard  
337 deviation, and probability density values are weighted by leaf area index. See Fig. 1 for the acronyms.

338 Fig. 12 demonstrates the global distributions of the MLA quality indicators. The global mean proportion of high-quality  
339 BRDF inputs is 68.03%. Northern South America and Central Africa have a low proportion of high-quality inputs (20%)  
340 because of cloud contamination (Fig. 12 (a)). Considering the large number of observations for each pixel (7904 from 2001  
341 to 2022), this percentage (20%) of high-quality observations is sufficient to map MLA. In addition, 80.39% of the global  
342 MLA map was derived within the feature ranges of training samples, and the rest 19.61% were mainly located in high-  
343 latitude regions and Africa. For the latter areas, the MLA map was predicted with extrapolation and caution should be taken  
344 when using the map (Fig. 12 (b)).



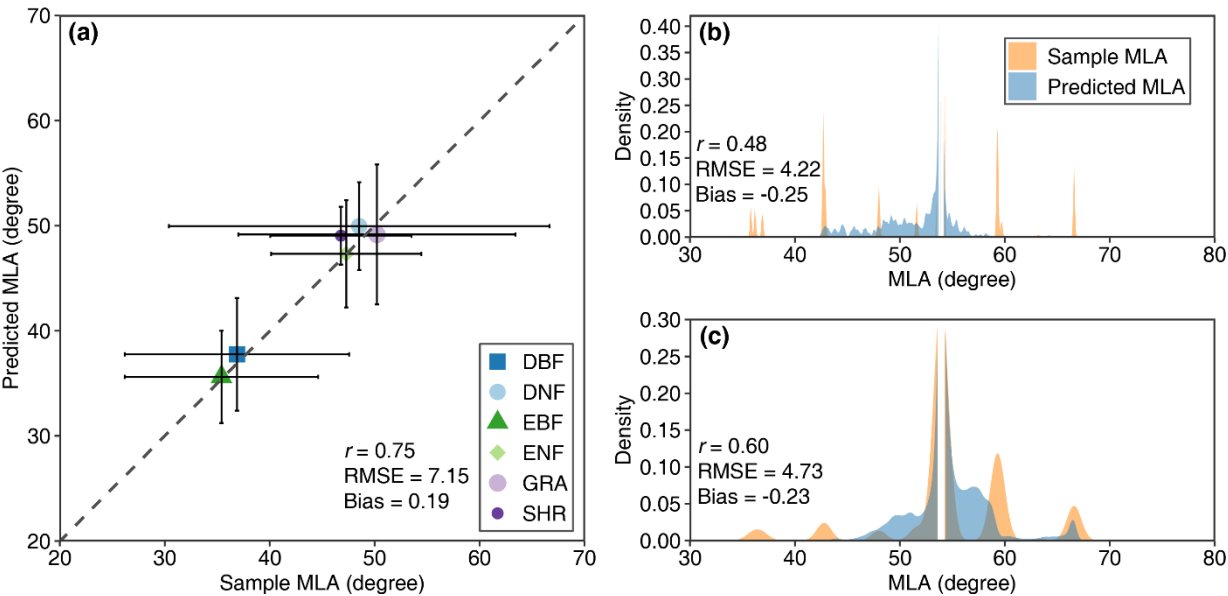
345

346 **Figure 12.** Global distributions of quality indicators. (a) and (b) denote the proportion of high-quality BRDF inversions, and whether the  
 347 prediction is within the ranges of training samples, respectively.

### 348 3.4 Evaluation of global MLA

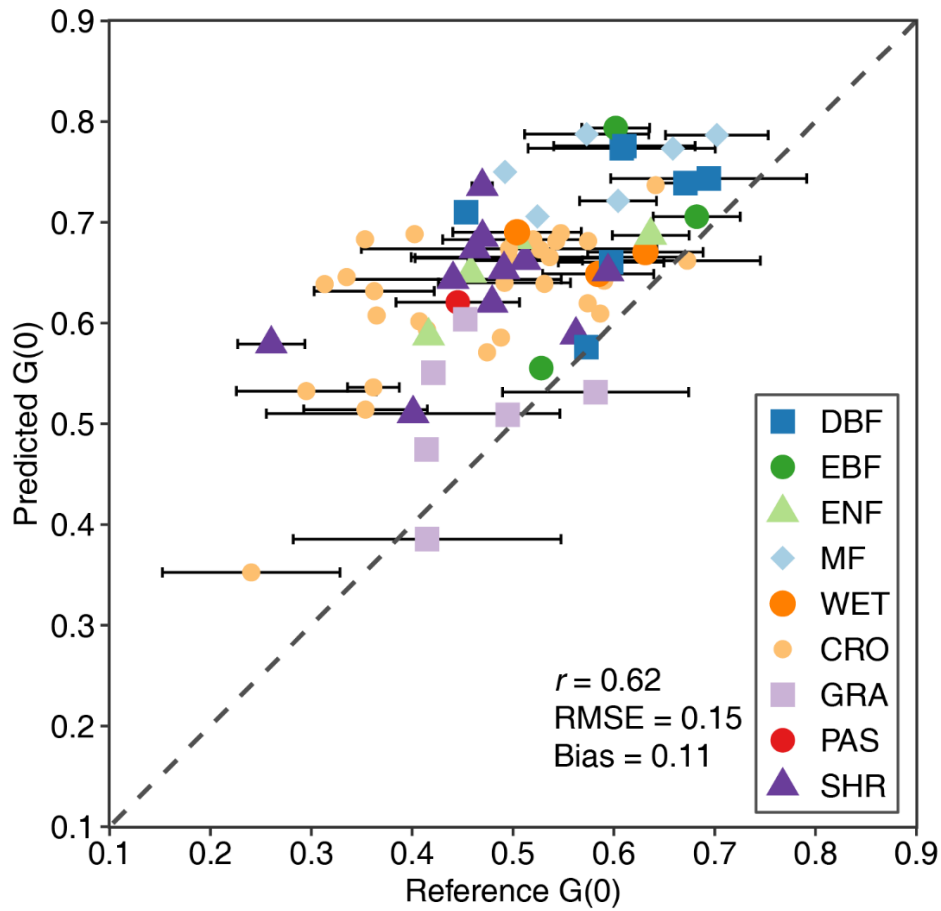
349 Fig. 13 shows the comparison between the predicted MLA and upscaled MLA samples using the ten-fold cross-validation  
 350 method. For noncrops, the predicted MLA is moderately consistent with the upscaled sample MLA ( $r = 0.75$ ,  $RMSE =$   
 351  $7.15^\circ$ ), with 83% of samples having residuals  $< 10^\circ$  and 94% of samples having residuals  $< 15^\circ$ . For DNF and SHR, the

352 predicted MLA compresses the variation range of sample MLA (Fig. 13a). For crops, the predicted MLA of CRO-C shows  
 353 higher consistency ( $r = 0.60$ ) than that of CRO-B ( $r = 0.48$ ). (Fig. 13b and c).



354  
 355 **Figure 13.** Comparisons between predicted MLA and sample MLA for noncrop (a), broadleaf crops (b), and cereal crops (c) (See Fig. 1  
 356 for the acronyms). The error bar in (a) represents the standard deviation.

357 Fig. 14 compares  $G(0)$  derived from the MLA and high-resolution reference data. The MLA-derived  $G(0)$  shows moderate  
 358 consistency with the reference  $G(0)$  ( $r = 0.62$ ), and 65% of the estimated  $G(0)$  residuals are  $< 0.15$ , and 84% of the residuals  
 359 are  $< 0.20$ . The estimated  $G(0)$  generally overestimates (bias = 0.11), especially when  $G(0)$  is low ( $< 0.60$ ), mainly for crops,  
 360 pasture, woody wetlands, and shrubs, whereas grasslands show better consistency. The estimated  $G(0)$  is temporally more  
 361 stable than the reference  $G(0)$  which is generally greater than 0.50 and displays seasonal variation (horizontally distributed  
 362 bars in Fig. 14).



363  
 364 **Figure 14.** Comparisons of  $G(0)$  derived from mean leaf inclination angle and high-resolution reference data for different plant functional  
 365 types (see Fig. 2 for the acronyms). The error bar represents the standard deviation of reference  $G(0)$  at different seasons.

## 366 4 Discussion

### 367 4.1 Global MLA and $G(0)$

368 This study compiled global LIA field measurements and generated the first global 500 m MLA and  $G(0)$  maps (Figs. 8 and  
 369 10). These maps show the average MLA and  $G(0)$  conditions during the growing seasons from 2001 to 2022. Overall, the  
 370 global MLA is lowest around the equator and increases with latitude (Figs. 8 and 10). This accords with the MLA latitude  
 371 variation derived from model simulations ([Huemmrich, 2013](#)). Crops have higher MLA than broadleaf forests whose leaves  
 372 are relatively horizontal. The global MLA and  $G(0)$  maps enhance our understanding of the global distribution of MLA and  
 373  $G(0)$  and should be useful in radiative transfer modeling, remote sensing of vegetation parameters, land surface modeling,  
 374 and ecological studies.

375 The global MLA shows good consistency with validation samples (Fig. 13) and the statistics of LIA field measurements  
 376 (Tables 3 and 4), demonstrating its reliability. The globally derived MLA is 41.47°, which is consistent with the LIA  
 377 measurements (40.74°, Tables 3 and 4). However, the derived MLAs of DBF, DNF, CRO-B, and SHR are approximately 10°  
 378 greater than the measured MLAs. It is noted that the number and spatial distribution of LIA measurements for these biomes  
 379 are limited. For example, the global CRO-B areas are dominated by soybeans with higher LIA (Table S2), and the LIA  
 380 measurements for soybeans are limited, which caused the CRO-B MLA in the global map to be greater than that in the  
 381 measurement statistics (Tables 3 and 4). The poor crop MLA prediction (Fig. 13b) is mainly caused by a small number of  
 382 samples and the strong seasonal variation. It is difficult to consider within-crop LIA variation when typical MLA values are  
 383 assigned to different crops.

384 Due to the lack of high-resolution reference MLA, the global MLA was evaluated through a comparison of the MLA-derived  
 385  $G(0)$  with the high-resolution reference  $G(0)$  (Fig. 14). This practice was adopted because both MLA and  $G(0)$  are closely  
 386 related.  $G(0)$  is typically calculated from the LIA distribution function based on Nilson's algorithm ([Nilson, 1971](#)). We  
 387 calculated  $G(0)$  from MLA assuming an ellipsoidal LIA distribution ([De Wit, 1965](#)) and found that the calculated  $G(0)$  is  
 388 highly consistent with the reference  $G(0)$  calculated from the Nilson's algorithm for different theoretical LIA distributions  
 389 (Fig. S5). The MLA-calculated  $G(0)$  also shows a monotonic decreasing relationship with MLA (Fig. S6).

390 The result shows medium consistency but MLA-derived  $G(0)$  overestimates at low values ( $< 0.60$ ), especially for CRO, PAS,  
 391 SHR, and WET. The overestimation may be partly caused by the underestimation of MLA at high values that is related to  
 392 the errors introduced in the sample expansion and upscaling. These errors are mainly caused by a lack of LIA measurements,  
 393 vegetation structural complexity, and seasonal variation. In addition, the uncertainties in the reference  $G(0)$  may have  
 394 contributed to the overestimation. The reference  $G(0)$  was derived from the Beer-Lambert law (Eq. (4)) which assumes that  
 395 the canopy is a turbid medium. The turbid medium assumption is unrealistic for complex vegetation ([Widlowski et al., 2014](#)).  
 396 The angular variation of CI and the mixture of branches and leaves in generating high-resolution  $G(0)$  can also lead to the  
 397 overestimation. Previous studies have shown that CI increases with the view zenith angle ([Fang, 2021](#)), which means that the  
 398 whole  $CI > CI(0)$  and can lead to the underestimation of the reference  $G(0)$  (Eq. (6) and (7)). The mixture of branches and  
 399 leaves may result in the underestimation of the reference  $G(0)$  due to the usually higher inclination angle of the trunks ([Liu et al., 2019](#)).  
 400 The MODIS LAI product used for LIA upscaling in the  $G(0)$  validation (section 2.4) is known to have issues such  
 401 as internal inconsistency, backup algorithm accuracy, and spatiotemporal gaps ([Kandasamy et al., 2013](#); [Pu et al., 2023](#);  
 402 [Zhang et al., 2024](#)). In the future, new improved MODIS LAI can be used in the  $G(0)$  validation ([Pu et al., 2024](#); [Yan et al., 2024](#)).  
 403 Compared with the previous  $G(0)$  derived from global vegetation biophysical products (Eq. (7)) ( $R^2 = 0.11$ , RMSE =  
 404 0.53) ([Li et al., 2022](#)), the MLA-derived  $G(0)$  performs better ( $R = 0.62$ , RMSE = 0.15). In addition, the  $G(0)$  data obtained  
 405 from our study can be used to derive the  $G(\theta)$  for any arbitrary angle. One method of getting  $G(\theta)$  is based on single-  
 406 parameter ellipsoidal leaf angle distribution ([Campbell, 1990](#)) (Eq. (3)). Another method is to make use of both  $G(0)$  and  
 407  $G(57.3^\circ) (\equiv 0.5)$  and derive  $G(\theta)$  using a simple linear ( $G(\theta) = a \cdot \theta + b$ ) or sinusoidal ( $G(\theta) = a \cdot \sin(\theta) + b$ )

408 interpolation method. Since  $G(\theta)$  varies most significantly in the nadir direction for different MLA ([Wilson, 1959](#)), the  
409 uncertainty of  $G(\theta)$  derived from the global MLA in other directions will be smaller than that of  $G(0)$ .

410

## 411 4.2 The relationship between MLA and other variables

412 Analysis of the relationships between MLA and other features in the MLA mapping process reveals that MLA is negatively  
413 correlated with NDVI, NIR reflectance, and NIR BRDF kernel coefficients (Fig. 7). These findings are consistent with other  
414 simulation and experimental studies ([Zou and Möttus, 2015](#); [Liu et al., 2012](#); [Dong et al., 2019](#); [Jacquemoud et al., 1994](#)).  
415 Higher MLA means lower radiation interception, more NIR and red downward radiations reach the soil background. This  
416 causes lower NIR and higher red reflectance because the soil background typically has lower (higher) reflectance for NIR  
417 (red) ([Siegmond and Menz, 2005](#)). This results in negative correlations between MLA and NIR reflectance and NDVI ([Liu et](#)  
418 [al., 2012](#)). The negative relationships between MLA and radiation, precipitation, and temperature (Fig. 7) are related to the  
419 vegetation adaptation mechanism. Under suitable climate conditions (radiation, precipitation, and temperature), horizontal  
420 leaves are formed to absorb more radiation and increase the photosynthesis rate ([Van Zanten et al., 2010](#); [King, 1997](#)). The  
421 positive correlation between MLA and the standard deviation of radiation and temperature (Fig. 7) indicates that the MLA is  
422 more vertical in areas with significant seasonal changes in radiation and temperature (mid to high-latitude areas) because  
423 vertical leaves maximize intercepted radiation under low solar altitudes at mid to high-latitude areas ([Huemmrich, 2013](#)).  
424 Plant function type was initially used as a predictive variable (Tables 1 and 2), but relatively low importance was found for  
425 LIA prediction (Fig.6, ranked 47 out of 76). This may be because the biome information is implicitly included in the spectral  
426 features as the former is frequently derived from the latter ([Sulla-Menashe et al., 2019](#)). Previous studies have demonstrated  
427 that the LIA variation within PFTs may be larger than that between PFTs. This indicates that the PFT is not a good predictor  
428 ([Prentice et al., 2024](#)). To avoid overfitting, only the most important 40 features were used for MLA prediction (Fig. 6). To  
429 explore the regional differences of the variable importance, an analysis was conducted for the tropical (23.5°S-23.5°N),  
430 northern temperate (23.5°N-60°N), northern polar (60°N-90°N), and the southern temperate (23.5°S-60°S) zones. The 40  
431 most important variables are similar among different regions although minor differences exist (Fig. S7). Among the 40  
432 variables for tropical, northern temperate, northern polar, and southern temperate zones, 32, 35, 30, and 31 of them,  
433 respectively, are the same as the 40 global variables (Fig. S7). Climate and spectral variables are significant among all  
434 regions, whereas BRDF features are the most important in the southern temperate zone. The 40 most important variables in  
435 the global MLA prediction account for ~ 80% of total importance among different regions, which is similar to that in the  
436 global prediction.

## 437 4.3 Use of the new MLA map

438 The spherical LAD assumption has been widely adopted in the literature ([Tang et al., 2016](#); [Zhao et al., 2020](#); [Wang and](#)  
439 [Fang, 2020](#)). This study demonstrates that the spherical assumption is valid only for cereal crops, but not for broadleaf



440 forests (Tables 3 and 4). This finding is consistent with previous local LIA measurements ([De Wit, 1965](#); [Pisek et al., 2013](#);  
441 [Yan et al., 2021](#)). For crops, the spherical assumption may even become invalid because of seasonality and species diversity  
442 (Table S2, Figs. 5 and 9). Fig. 14 shows that most of the reference  $G(0)$  values are greater than 0.50, while the spherical  
443 distribution would underestimate the interception of radiation and rainfall (Figs. 9 and 11) ([Stadt and Loeffers, 2000](#)). In  
444 current LSMs, a constant LIA is commonly assigned for each PFT ([Majasalmi and Bright, 2019](#)). For example, the  
445 Community Land Model V5 (CLM5) (Table S4) ([Lawrence et al., 2019](#)) uses lower inclination indices and higher LIA  
446 values than our results (Tables 3 and 4) and thus may underestimate canopy interception. The global LIA map generated in  
447 this study provides a more reasonable LIA parameterization strategy for the application communities.

#### 448 4.4 Limitations and prospects

449 The limitations of this study mainly relate to the small number of LIA measurements, especially continuous measurements.  
450 First, within-species LIA variations were neglected in the spatial expansion due to limited spatial coverage of existing LIA-  
451 measured data (Section 2.3.1). This may introduce some errors, especially for crops. Second, three different sources of LIA  
452 measurements were gathered with different measurement schemes, and uncertainty may arise because of these differences.  
453 The random forest algorithm is robust to these differences because part of the samples and features were randomly selected  
454 and the algorithm ensembled the predictions from multiple decision trees ([Svetnik et al., 2003](#)). We manually inspected all  
455 field LIA data and are confident in their data quality. Third, for forests, the contribution of the understory was not considered.  
456 Typically, the understory is characterized by more horizontal leaves, and ignoring the understory may lead to an MLA  
457 overestimation ([Utsugi et al., 2006](#)). Nevertheless, a previous study showed that the relative contribution of the understory to  
458 the overall MLA is less than 10% ([Li et al., 2022](#)). Finally, only the growing season MLA was calculated, whereas the  
459 seasonal and long-term variations of MLA were not considered due to the lack of continuous LIA measurements.

460 We assumed a linear LAI-EVI2 relationship ( $LAI = a \cdot EVI2$ ) to upscale MLA from the canopy to 500 m scale (Section 2.3.1  
461 and Appendix A). Global analysis of MODIS LAI and EVI2 products shows a slight non-linear relationship between them  
462 (Fig. S8). The non-linear relationship was also used to upscale MLA (Eq. A2) in a side experiment, where the derived MLA  
463 was found consistent with the original one (Fig. S9) because of the homogeneity of the 500 m pixel after rigorous sample  
464 screening (section 2.3.1). This demonstrates the suitability of the linear assumption.

465 In the future, more efficient LIA observation systems should be developed to provide continuous LIA data ([Kattenborn et al.,  
466 2022](#)). LIA measurements can be integrated into existing ground observation networks, such as the National Ecological  
467 Observatory Network (NEON) ([Kao et al., 2012](#)), Integrated Carbon Observation System (ICOS) ([Gielen et al., 2018](#)), and  
468 Terrestrial Ecosystem Research Network (TERN) ([Karan et al., 2016](#)), to enhance temporal LIA measurements in larger  
469 spatial extent, especially for DNF and crops. Using standard LIA measurement protocols will certainly improve the LIA data  
470 consistency. ([Li et al., 2023](#)). In addition, canopy structure parameters are interrelated, and introducing other structure  
471 parameter products, such as LAI, FVC, CI, and canopy height as predictive variables may improve the MLA prediction.  
472 Multiangle reflectance ([Jacquemoud et al., 2009](#); [Goel and Thompson, 1984](#); [Jacquemoud et al., 1994](#)) or light detection and

473 ranging ([Zheng and Moskal, 2012](#); [Bailey and Mahaffee, 2017](#); [Itakura and Hosoi, 2019](#)) are encouraging remote sensing  
474 tools that can help to derive temporally continuous and high-resolution MLA data.

## 475 **5 Conclusion**

476 This study compiled existing global LIA measurements and generated the first global 500 m MLA and G(0) products by  
477 gap-filling the LIA measurement data using a random forest regressor. The mean of global LIA measurements is 40.74° and  
478 cereal crops show the highest MLA (59.11°). The global MLA shows an explicit spatial distribution and the value increases  
479 with latitude. The global MLA is  $41.47^{\circ} \pm 9.55^{\circ}$  and follows the order of CRO-C > CRO-B > DNF > SHR > ENF  $\approx$  GRA >  
480 DBF > EBF. The predicted MLA presents a medium consistency ( $r = 0.75$ , RMSE = 7.15°) with the validation samples for  
481 noncrops. For crops, the results are relatively poorer ( $r = 0.48$  and 0.60 for broadleaf crops and cereal crops) because of  
482 limited LIA measurements and strong seasonality. The G(0) derived from MLA is moderately consistent with the reference  
483 G(0) ( $r = 0.62$ ).

484 The MLA and G(0) products obtained in this study would enhance our understanding of global LIA and assist remote  
485 sensing retrieval and land surface modeling studies. These products provide a more realistic parameterization strategy than  
486 the commonly used spherical LAD and PFT-specific MLA assignment. Note the global MLA and G(0) products mainly  
487 represent the typical state during the growing season. These products can be further improved and temporal MLA data can  
488 be obtained through continuous measurements and remote sensing retrieval.

## 489 **Data availability**

490 The global MLA and G(0) products (CAS-GLA) are available in: Li, S. and Fang, H. 2024,  
491 <https://doi.org/10.5281/zenodo.12739662>([Li and Fang, 2025](#)). The related code can be accessed at  
492 [https://code.earthengine.google.com/?accept\\_repo=users/SiJia/MTA](https://code.earthengine.google.com/?accept_repo=users/SiJia/MTA).

## 493 **Author contributions**

494 HF and SL conceptualized this work. SL compiled global LIA measurements, generated global products, and curated the  
495 datasets. SL and HF wrote the manuscript. HF was responsible for funding and supervision.

## 496 **Competing interests**

497 The contact author has declared that none of the authors has any competing interests.

## 498 Acknowledgements

499 The authors are grateful to TRY and many other researchers for sharing the LIA measurement data. Jens Kattge at the Max  
500 Planck Institute for Biogeochemistry and Dongliang Cheng at Fujian Normal University provided the TRY species location  
501 data and LIA measurements in China's subtropical regions, respectively.

## 502 Financial support

503 This work was mainly supported by the National Natural Science Foundation of China (42171358).

## 504 Appendix A. Upscaling LIA from leaf, canopy to ecosystem scale

505 From leaf to canopy scale, the entire canopy MLA is commonly calculated as the average of all measured leaf LIAs  
506 weighted by leaf area (Eq. A1) ([Zou et al., 2014](#); [De Wit, 1965](#); [Yan et al., 2021](#)). In practice, because of the difficulty in leaf  
507 area measurement, especially for a large number of leaves, the variability of leaf areas within a canopy is often ignored and  
508 the areas of all leaves are assumed similar. In this case, the canopy LIA can be simplified as the average LIA weighted by  
509 leaf number (Eq. A1) ([Ryu et al., 2010](#); [Pisek et al., 2011](#); [Chianucci et al., 2018](#)):

$$510 \quad MLA_{canopy} = \frac{\sum_i LIA_i * LA_i}{\sum_i LA_i} = \frac{LA_{mean} * \sum_i LIA_i}{LA_{mean} * N} = \frac{\sum_i LIA_i}{N} \quad (A1)$$

511 where  $MLA_{canopy}$  is the MLA at canopy scale,  $i$  is the  $i$ th leaf, LIA is leaf inclination angle, LA is single leaf area,  $LA_{mean}$  is  
512 the mean leaf area by ignoring the variation of leaf area within a canopy,  $N$  is number of leaves within a canopy.

513 From the canopy to 30 m scale, the canopy level MLA is regarded as equal to 30 m-MLA because for MLA measurements,  
514 the dominant species was artificially identified by investigators and the spatial representativeness at the extent of 30 m is  
515 ensured.

516 From 30 m to 500 m, the 500 m MLA was formulated as the weighted average of 30 m MLA by the leaf area of the 30 m  
517 pixel (Eq. A2), the same as that from the leaf to canopy scale. The leaf area of a 30 m pixel can be deduced from the product  
518 of leaf area index (LAI) and the ground area of a 30 m pixel according to the definition of LAI (the half of green leaf area on  
519 the unit of ground area) (Eq. A2) ([Fang et al., 2019](#)).

$$520 \quad MLA_{500} = \frac{\sum_j MLA_{30-j} * LA_{30-j}}{\sum_j LA_{30-j}} = \frac{\sum_j MLA_{30-j} * LAI_{30-j} * S}{\sum_j LAI_{30-j} * S} = \frac{\sum_j MLA_{30-j} * LAI_{30-j}}{\sum_j LAI_{30-j}} \quad (A2)$$

521 Where  $MLA_{500}$  and  $MLA_{30}$  represent MLA at 500 m and 30 m scales,  $j$  is the  $j$ th 30 m pixel,  $LA_{30-j}$  is the total leaf area of a  
522 30 m pixel,  $LAI_{30-j}$  is leaf area index (m<sup>2</sup>/m<sup>2</sup>) of a 30 m pixel,  $S$  is the ground area of a 30 m pixel.

523 Assuming  $LAI = a * EVI2 + b$  and  $b \approx 0$  (as illustrated in Fig. S8), the MLA at 500 m scale can be calculated as:

524

$$MLA_{500} = \frac{\sum_j MLA_{30\_j} * EVI2_{30\_j}}{\sum_j EVI2_{30\_j}}$$

(A3)

525

526 **References**

527 Alexandridis, T. K., Ovakoglou, G., and Clevers, J. G. P. W.: Relationship between MODIS EVI and LAI across time and  
528 space, *Geocarto International*, 35, 1385-1399, 10.1080/10106049.2019.1573928, 2019.

529 Bailey, B. N. and Mahaffee, W. F.: Rapid measurement of the three-dimensional distribution of leaf orientation and the leaf  
530 angle probability density function using terrestrial LiDAR scanning, *Remote Sens. Environ.*, 194, 63-76,  
531 10.1016/j.rse.2017.03.011, 2017.

532 Bayat, B., van der Tol, C., and Verhoef, W.: Integrating satellite optical and thermal infrared observations for improving  
533 daily ecosystem functioning estimations during a drought episode, *Remote Sens. Environ.*, 209, 375-394,  
534 10.1016/j.rse.2018.02.027, 2018.

535 Boryan, C., Yang, Z., Mueller, R., and Craig, M.: Monitoring US agriculture: the US department of agriculture, national  
536 agricultural statistics service, cropland data layer program, *Geocarto International*, 26, 341-358, 2011.

537 Brown, L. A., Meier, C., Morris, H., Pastor-Guzman, J., Bai, G., Lerebourg, C., Gobron, N., Lanconelli, C., Clerici, M., and  
538 Dash, J.: Evaluation of global leaf area index and fraction of absorbed photosynthetically active radiation products over  
539 North America using Copernicus Ground Based Observations for Validation data, *Remote Sens. Environ.*, 247,  
540 10.1016/j.rse.2020.111935, 2020.

541 Campbell, G.: Derivation of an angle density function for canopies with ellipsoidal leaf angle distributions, *Agricultural and  
542 forest meteorology*, 49, 173-176, 1990.

543 Chen, J. M., Ju, W., Ciais, P., Viovy, N., Liu, R., Liu, Y., and Lu, X.: Vegetation structural change since 1981 significantly  
544 enhanced the terrestrial carbon sink, *Nat Commun*, 10, 4259, 10.1038/s41467-019-12257-8, 2019.

545 Chen, X., Zhong, Q.-L., Lyu, M., Wang, M., Hu, D., Sun, J., and Cheng, D.: Trade-off relationship between light  
546 interception and leaf water shedding at different canopy positions of 73 broad-leaved trees of Yangji Mountain in Jiangxi  
547 Province, China, *SCIENTIA SINICA Vitae*, 51, 91-101, 10.1360/SSV-2020-0218, 2021.

548 Chianucci, F., Pisek, J., Raabe, K., Marchino, L., Ferrara, C., and Corona, P.: A dataset of leaf inclination angles for  
549 temperate and boreal broadleaf woody species, *Annals of Forest Science*, 75, 50-50, 10.1007/s13595-018-0730-x, 2018.

550 Crawford, C. J., Roy, D. P., Arab, S., Barnes, C., Vermote, E., Hulley, G., Gerace, A., Choate, M., Engebretson, C.,  
551 Micijevic, E., Schmidt, G., Anderson, C., Anderson, M., Bouchard, M., Cook, B., Dittmeier, R., Howard, D., Jenkerson, C.,  
552 Kim, M., Kleyians, T., Maersperger, T., Mueller, C., Neigh, C., Owen, L., Page, B., Pahlevan, N., Rengarajan, R., Roger, J.-  
553 C., Sayler, K., Scaramuzza, P., Skakun, S., Yan, L., Zhang, H. K., Zhu, Z., and Zahn, S.: The 50-year Landsat collection 2  
554 archive, *Science of Remote Sensing*, 8, 100103, <https://doi.org/10.1016/j.srs.2023.100103>, 2023.

555 d'Andrimont, R., Verhegghen, A., Lemoine, G., Kempeneers, P., Meroni, M., and van der Velde, M.: From parcel to  
556 continental scale – A first European crop type map based on Sentinel-1 and LUCAS Copernicus in-situ observations,  
557 *Remote Sens. Environ.*, 266, 112708, <https://doi.org/10.1016/j.rse.2021.112708>, 2021.

558 de Wit, C. T.: *Photosynthesis of leaf canopies*, Pudoc, 1965.

559 Dong, J., fu, y., wang, j., Tian, H., Fu, S., Niu, Z., Han, W., Zheng, Y., Huang, J., and Yuan, W.: 30m winter wheat  
560 distribution map of China for four years (2016-2019), 10.6084/m9.figshare.12003990.v2, 2020.

561 Dong, T., Liu, J., Shang, J., Qian, B., Ma, B., Kovacs, J. M., Walters, D., Jiao, X., Geng, X., and Shi, Y.: Assessment of red-  
562 edge vegetation indices for crop leaf area index estimation, *Remote Sens. Environ.*, 222, 133-143, 10.1016/j.rse.2018.12.032,  
563 2019.

564 Fang, H.: Canopy clumping index (CI): A review of methods, characteristics, and applications, *Agricultural and Forest*  
565 *Meteorology*, 303, 108374, <https://doi.org/10.1016/j.agrformet.2021.108374>, 2021.

566 Fang, H., Baret, F., Plummer, S., and Schaepman-Strub, G.: An Overview of Global Leaf Area Index (LAI): Methods,  
567 Products, Validation, and Applications, *Rev. Geophys.*, 57, 739-799, 10.1029/2018rg000608, 2019.

568 Fang, H., Li, S., Zhang, Y., Wei, S., and Wang, Y.: New insights of global vegetation structural properties through an  
569 analysis of canopy clumping index, fractional vegetation cover, and leaf area index, *Science of Remote Sensing*, 100027,  
570 <https://doi.org/10.1016/j.srs.2021.100027>, 2021.

571 Fisette, T., Rollin, P., Aly, Z., Campbell, L., Daneshfar, B., Filyer, P., Smith, A., Davidson, A., Shang, J., and Jarvis, I.:  
572 AAFC annual crop inventory, 2013 Second International Conference on Agro-Geoinformatics (Agro-Geoinformatics), 270-  
573 274,

574 Foley, J. A., Prentice, I. C., Ramankutty, N., Levis, S., Pollard, D., Sitch, S., and Haxeltine, A.: An integrated biosphere  
575 model of land surface processes, terrestrial carbon balance, and vegetation dynamics, *Global biogeochemical cycles*, 10,  
576 603-628, 1996.

577 Gao, S., Zhong, R., Yan, K., Ma, X., Chen, X., Pu, J., Gao, S., Qi, J., Yin, G., and Myneni, R. B.: Evaluating the saturation  
578 effect of vegetation indices in forests using 3D radiative transfer simulations and satellite observations, *Remote Sens.*  
579 *Environ.*, 295, 10.1016/j.rse.2023.113665, 2023.

580 Gielen, B., Acosta, M., Altimir, N., Buchmann, N., Cescatti, A., Ceschia, E., Fleck, S., Hörtnagl, L., Klumpp, K., Kolari, P.,  
581 Lohila, A., Loustau, D., Mara  n-Jimenez, S., Manise, T., Matteucci, G., Merbold, L., Metzger, C., Moureaux, C.,  
582 Montagnani, L., Nilsson, M. B., Osborne, B., Papale, D., Pavelka, M., Saunders, M., Simioni, G., Soudani, K., Sonnentag,  
583 O., Tallec, T., Tuittila, E.-S., Peichl, M., Pokorny, R., Vincke, C., and Wohlfahrt, G.: Ancillary vegetation measurements at  
584 ICOS ecosystem stations, *International Agrophysics*, 32, 645-664, 10.1515/intag-2017-0048, 2018.

585 Goel, N. S. and Thompson, R. L.: Inversion of vegetation canopy reflectance models for estimating agronomic variables. V.  
586 Estimation of leaf area index and average leaf angle using measured canopy reflectances, *Remote Sens. Environ.*, 16, 69-85,  
587 10.1016/0034-4257(84)90028-2, 1984.

588 Han, J., Zhang, Z., Luo, Y., Cao, J., Zhang, L., Cheng, F., Zhuang, H., Zhang, J., and Tao, F.: NESEA-Rice10: high-  
589 resolution annual paddy rice maps for Northeast and Southeast Asia from 2017 to 2019, *Earth System Science Data*, 13,  
590 5969-5986, 10.5194/essd-13-5969-2021, 2021.

591 Hinojo-Hinojo, C. and Goulden, M.: A compilation of canopy leaf inclination angle measurements across plant species and  
592 biome types, 10.7280/D1T97H, 2020.

593 Huemmrich, K. F.: Simulations of Seasonal and Latitudinal Variations in Leaf Inclination Angle Distribution: Implications  
 594 for Remote Sensing, *Advances in Remote Sensing*, 02, 93-101, 10.4236/ars.2013.22013, 2013.

595 Itakura, K. and Hosoi, F.: Estimation of Leaf Inclination Angle in Three-Dimensional Plant Images Obtained from Lidar,  
 596 *Remote Sensing*, 11, 10.3390/rs11030344, 2019.

597 Jacquemoud, S., Flasse, S., Verdebout, J., and Schmuck, G.: Comparison of Several Optimization Methods To Extract  
 598 Canopy Biophysical Parameters - Application To Caesar Data, 291-298, 1994.

599 Jacquemoud, S., Verhoef, W., Baret, F., Bacour, C., Zarco-Tejada, P. J., Asner, G. P., François, C., and Ustin, S. L.:  
 600 PROSPECT+SAIL models: A review of use for vegetation characterization, *Remote Sens. Environ.*, 113, S56-S66,  
 601 10.1016/j.rse.2008.01.026, 2009.

602 Kandasamy, S., Baret, F., Verger, A., Neveux, P., and Weiss, M.: A comparison of methods for smoothing and gap filling  
 603 time series of remote sensing observations—application to MODIS LAI products, *Biogeosciences*, 10, 4055-4071, 2013.

604 Kao, R. H., Gibson, C. M., Gallery, R. E., Meier, C. L., Barnett, D. T., Docherty, K. M., Blevins, K. K., Travers, P. D.,  
 605 Azuaje, E., Springer, Y. P., Thibault, K. M., McKenzie, V. J., Keller, M., Alves, L. F., Hinckley, E.-L. S., Parnell, J., and  
 606 Schimel, D.: NEON terrestrial field observations: designing continental-scale, standardized sampling, *Ecosphere*, 3, art115,  
 607 10.1890/es12-00196.1, 2012.

608 Karan, M., Liddell, M., Prober, S. M., Arndt, S., Beringer, J., Boer, M., Cleverly, J., Eamus, D., Grace, P., Van Gorsel, E.,  
 609 Hero, J. M., Hutley, L., Macfarlane, C., Metcalfe, D., Meyer, W., Pendall, E., Sebastian, A., and Wardlaw, T.: The  
 610 Australian SuperSite Network: A continental, long-term terrestrial ecosystem observatory, *Sci. Total Environ.*, 568, 1263-  
 611 1274, 10.1016/j.scitotenv.2016.05.170, 2016.

612 Kattenborn, T., Richter, R., Guimarães-Steinicke, C., Feilhauer, H., and Wirth, C.: AngleCam: Predicting the temporal  
 613 variation of leaf angle distributions from image series with deep learning, *Methods in Ecology and Evolution*, 13, 2531-2545,  
 614 10.1111/2041-210x.13968, 2022.

615 Kattge, J., Bonisch, G., Diaz, S., Lavorel, S., and Prentice, I. C.: TRY plant trait database - enhanced coverage and open  
 616 access, *Glob Chang Biol*, 26, 119-188, 10.1111/gcb.14904, 2020.

617 King, D. A.: The Functional Significance of Leaf Angle in Eucalyptus, *Aust. J. Bot.*, 45, 619-639,  
 618 <https://doi.org/10.1071/BT96063>, 1997.

619 Kuusk, A.: A two-layer canopy reflectance model, *Journal of Quantitative Spectroscopy and Radiative Transfer*, 71, 1-9,  
 620 [https://doi.org/10.1016/S0022-4073\(01\)00007-3](https://doi.org/10.1016/S0022-4073(01)00007-3), 2001.

621 Lang, A. R. G.: Leaf orientation of a cotton plant, *Agricultural Meteorology*, 11, 37-51, 10.1016/0002-1571(73)90049-6,  
 622 1973.

623 Lawrence, D. M., Fisher, R. A., Koven, C. D., Oleson, K. W., Swenson, S. C., Bonan, G., Collier, N., Ghimire, B., Van  
 624 Kampenhout, L., and Kennedy, D.: The Community Land Model version 5: Description of new features, benchmarking, and  
 625 impact of forcing uncertainty, *Journal of Advances in Modeling Earth Systems*, 11, 4245-4287, 2019.

Li, S. and Fang, H.: Global Leaf Inclination Angle (LIA) and Nadir Leaf Projection Function (G(0)) Products (1.1), Zenodo [dataset], 10.5281/zenodo.12739662, 2025.

Li, S., Fang, H., and Zhang, Y.: Determination of the Leaf Inclination Angle (LIA) through Field and Remote Sensing Methods: Current Status and Future Prospects, *Remote Sensing*, 15, 946, 2023.

Li, S., Fang, H., Zhang, Y., and Wang, Y.: Comprehensive evaluation of global CI, FVC, and LAI products and their relationships using high-resolution reference data, *Science of Remote Sensing*, 6, 10.1016/j.srs.2022.100066, 2022.

Liu, J., Pattey, E., and Jégo, G.: Assessment of vegetation indices for regional crop green LAI estimation from Landsat images over multiple growing seasons, *Remote Sens. Environ.*, 123, 347-358, 10.1016/j.rse.2012.04.002, 2012.

Liu, J., Wang, T., Skidmore, A. K., Jones, S., Heurich, M., Beudert, B., and Premier, J.: Comparison of terrestrial LiDAR and digital hemispherical photography for estimating leaf angle distribution in European broadleaf beech forests, *ISPRS Journal of Photogrammetry and Remote Sensing*, 158, 76-89, 10.1016/j.isprsjprs.2019.09.015, 2019.

Maes, W. and Steppe, K.: Estimating evapotranspiration and drought stress with ground-based thermal remote sensing in agriculture: a review, *J. Exp. Bot.*, 63, 4671-4712, 2012.

Majasalmi, T. and Bright, R. M.: Evaluation of leaf-level optical properties employed in land surface models – example with CLM 5.0, *Geoscientific Model Development Discussions*, 1-24, 2019.

Mantilla-Perez, M. B. and Salas Fernandez, M. G.: Differential manipulation of leaf angle throughout the canopy: current status and prospects, *J. Exp. Bot.*, 68, 5699-5717, 2017.

Moreno-Martínez, Á., Camps-Valls, G., Kattge, J., Robinson, N., Reichstein, M., van Bodegom, P., Kramer, K., Cornelissen, J. H. C., Reich, P., Bahn, M., Niinemets, Ü., Peñuelas, J., Craine, J. M., Cerabolini, B. E. L., Minden, V., Laughlin, D. C., Sack, L., Allred, B., Baraloto, C., Byun, C., Soudzilovskaia, N. A., and Running, S. W.: A methodology to derive global maps of leaf traits using remote sensing and climate data, *Remote Sens. Environ.*, 218, 69-88, 10.1016/j.rse.2018.09.006, 2018.

Muñoz-Sabater, J., Dutra, E., Agustí-Panareda, A., Albergel, C., Arduini, G., Balsamo, G., Boussetta, S., Choulga, M., Harrigan, S., Hersbach, H., Martens, B., Miralles, D. G., Piles, M., Rodríguez-Fernández, N. J., Zsoter, E., Buontempo, C., and Thépaut, J.-N.: ERA5-Land: a state-of-the-art global reanalysis dataset for land applications, *Earth System Science Data*, 13, 4349-4383, 10.5194/essd-13-4349-2021, 2021.

Myneni, R., Knyazikhin, Y., Park, T.: MCD15A2H MODIS/Terra+Aqua Leaf Area Index/FPAR 8-day L4 Global 500m SIN Grid V006 [dataset], <http://doi.org/10.5067/MODIS/MCD15A2H.006>, 2015.

Nilson, T.: A theoretical analysis of the frequency of gaps in plant stands, *Agricultural Meteorology*, 8, 25-38, 1971.

Norman, J. M. and Campbell, G. S.: Canopy structure, in: *Plant Physiological Ecology: Field methods and instrumentation*, edited by: Pearcy, R. W., Ehleringer, J. R., Mooney, H. A., and Rundel, P. W., Springer Netherlands, Dordrecht, 301-325, 10.1007/978-94-009-2221-1\_14, 1989.

Pisek, J. and Adamson, K.: Dataset of leaf inclination angles for 71 different Eucalyptus species, *Data Brief*, 33, 106391, 10.1016/j.dib.2020.106391, 2020.



660 Pisek, J., Ryu, Y., and Alikas, K.: Estimating leaf inclination and G-function from leveled digital camera photography in  
661 broadleaf canopies, *Trees*, 25, 919-924, 10.1007/s00468-011-0566-6, 2011.

662 Pisek, J., Sonnentag, O., Richardson, A. D., and Möttus, M.: Is the spherical leaf inclination angle distribution a valid  
663 assumption for temperate and boreal broadleaf tree species?, *Agricultural and Forest Meteorology*, 169, 186-194,  
664 10.1016/j.agrformet.2012.10.011, 2013.

665 Pisek, J., Diaz-Pines, E., Matteucci, G., Noe, S., and Rebmann, C.: On the leaf inclination angle distribution as a plant trait  
666 for the most abundant broadleaf tree species in Europe, *Agricultural and Forest Meteorology*, 323,  
667 10.1016/j.agrformet.2022.109030, 2022.

668 Prentice, I. C., Balzarolo, M., Bloomfield, K. J., Chen, J. M., Dechant, B., Ghent, D., Janssens, I. A., Luo, X., Morfopoulos,  
669 C., Ryu, Y., Vicca, S., and van Hoolst, R.: Principles for satellite monitoring of vegetation carbon uptake, *Nature Reviews*  
670 *Earth & Environment*, 5, 818-832, 10.1038/s43017-024-00601-6, 2024.

671 Pu, J., Yan, K., Roy, S., Zhu, Z., Rautiainen, M., Knyazikhin, Y., and Myneni, R. B.: Sensor-independent LAI/FPAR CDR:  
672 reconstructing a global sensor-independent climate data record of MODIS and VIIRS LAI/FPAR from 2000 to 2022, *Earth*  
673 *System Science Data*, 16, 15-34, 10.5194/essd-16-15-2024, 2024.

674 Pu, J., Yan, K., Gao, S., Zhang, Y., Park, T., Sun, X., Weiss, M., Knyazikhin, Y., and Myneni, R. B.: Improving the MODIS  
675 LAI compositing using prior time-series information, *Remote Sens. Environ.*, 287, 10.1016/j.rse.2023.113493, 2023.

676 Raabe, K., Pisek, J., Sonnentag, O., and Annuk, K.: Variations of leaf inclination angle distribution with height over the  
677 growing season and light exposure for eight broadleaf tree species, *Agricultural and Forest Meteorology*, 214-215, 2-11,  
678 10.1016/j.agrformet.2015.07.008, 2015.

679 Ross, J.: Radiative transfer in plant communities, *Vegetation and the Atmosphere*, 13-55, 1975.

680 Ross, J.: The radiation regime and architecture of plant stands, 3, Springer Science & Business Media 1981.

681 Ryu, Y., Sonnentag, O., Nilson, T., Vargas, R., Kobayashi, H., Wenk, R., and Baldocchi, D. D.: How to quantify tree leaf  
682 area index in an open savanna ecosystem: A multi-instrument and multi-model approach, *Agricultural and Forest*  
683 *Meteorology*, 150, 63-76, 10.1016/j.agrformet.2009.08.007, 2010.

684 Schaaf, C. and Wang, Z.: MCD43A4 MODIS/Terra+Aqua BRDF/Albedo Nadir BRDF Adjusted Ref Daily L3 Global -  
685 500m V006, NASA EOSDIS Land Processes Distributed Active Archive Center [dataset],  
686 <https://doi.org/10.5067/MODIS/MCD43A4.006>, 2015a.

687 Schaaf, C. and Wang, Z.: MCD43A1 MODIS/Terra+Aqua BRDF/Albedo Model Parameters Daily L3 Global - 500m V006,  
688 NASA EOSDIS Land Processes Distributed Active Archive Center [dataset],  
689 <https://doi.org/10.5067/MODIS/MCD43A1.006>, 2015b.

690 Sellers, P. J.: Canopy reflectance, photosynthesis and transpiration, *International Journal of Remote Sensing*, 6, 1335-1372,  
691 10.1080/01431168508948283, 1985.

692 Shen, R., Dong, J., Yuan, W., Han, W., Ye, T., and Zhao, W.: A 30-m Resolution Distribution Map of Maize for China  
693 Based on Landsat and Sentinel Images, *Journal of Remote Sensing*, 2022, doi:10.34133/2022/9846712, 2022.

694 Siegmund, A. and Menz, G.: Fernes nah gebracht–Satelliten-und Luftbildeinsatz zur Analyse von Umweltveränderungen im  
695 Geographieunterricht, *Geographie und Schule*, 154, 2-10, 2005.

696 Stadt, K. J. and Lieffers, V. J.: MIXLIGHT: a flexible light transmission model for mixed-species forest stands, *Agricultural*  
697 *and Forest Meteorology*, 102, 235-252, 2000.

698 Sulla-Menashe, D., Gray, J. M., Abercrombie, S. P., and Friedl, M. A.: Hierarchical mapping of annual global land cover  
699 2001 to present: The MODIS Collection 6 Land Cover product, *Remote Sens. Environ.*, 222, 183-194,  
700 10.1016/j.rse.2018.12.013, 2019.

701 Svetnik, V., Liaw, A., Tong, C., Culberson, J. C., Sheridan, R. P., and Feuston, B. P.: Random forest: a classification and  
702 regression tool for compound classification and QSAR modeling, *Journal of chemical information and computer sciences*, 43,  
703 1947-1958, 2003.

704 Tadono, T., Ishida, H., Oda, F., Naito, S., Minakawa, K., and Iwamoto, H.: Precise global DEM generation by ALOS  
705 PRISM, *ISPRS Annals of the Photogrammetry, Remote Sensing and Spatial Information Sciences*, 2, 71-76, 2014.

706 Tang, H., Ganguly, S., Zhang, G., Hofton, M. A., Nelson, R. F., and Dubayah, R.: Characterizing leaf area index (LAI) and  
707 vertical foliage profile (VFP) over the United States, *Biogeosciences*, 13, 239-252, 10.5194/bg-13-239-2016, 2016.

708 Toda, M., Ishihara, M. I., Doi, K., and Hara, T.: Determination of species-specific leaf angle distribution and plant area  
709 index in a cool-temperate mixed forest from UAV and upward-pointing digital photography, *Agricultural and Forest*  
710 *Meteorology*, 325, 10.1016/j.agrformet.2022.109151, 2022.

711 Utsugi, H., Araki, M., Kawasaki, T., and Ishizuka, M.: Vertical distributions of leaf area and inclination angle, and their  
712 relationship in a 46-year-old *Chamaecyparis obtusa* stand, *For. Ecol. Manage.*, 225, 104-112,  
713 <https://doi.org/10.1016/j.foreco.2005.12.028>, 2006.

714 van Zanten, M., Pons, T. L., Janssen, J. A. M., Voesenek, L. A. C. J., and Peeters, A. J. M.: On the Relevance and Control of  
715 Leaf Angle, *Crit. Rev. Plant Sci.*, 29, 300-316, 10.1080/07352689.2010.502086, 2010.

716 Verhoef, W., Jia, L., Xiao, Q., and Su, Z.: Unified Optical-Thermal Four-Stream Radiative Transfer Theory for  
717 Homogeneous Vegetation Canopies, *IEEE Transactions on Geoscience and Remote Sensing*, 45, 1808-1822,  
718 10.1109/TGRS.2007.895844, 2007.

719 Wang, W. M., Li, Z. L., and Su, H. B.: Comparison of leaf angle distribution functions: Effects on extinction coefficient and  
720 fraction of sunlit foliage, *Agricultural and Forest Meteorology*, 143, 106-122, 10.1016/j.agrformet.2006.12.003, 2007.

721 Wang, Y. and Fang, H.: Estimation of LAI with the LiDAR Technology: A Review, *Remote Sensing*, 12,  
722 10.3390/rs12203457, 2020.

723 Weiss, M. and Baret, F.: CAN-EYE V6.4.91 User Manual, [https://www6.paca.inrae.fr/can-](https://www6.paca.inrae.fr/can-eye/Documentation/Documentation)  
724 [eye/Documentation/Documentation](https://www6.paca.inrae.fr/can-eye/Documentation/Documentation), 2017.

725 Widlowski, J.-L., Côté, J.-F., and Béland, M.: Abstract tree crowns in 3D radiative transfer models: Impact on simulated  
726 open-canopy reflectances, *Remote Sens. Environ.*, 142, 155-175, 10.1016/j.rse.2013.11.016, 2014.

727 Wilson, J.: Inclined point quadrats, *New Phytol.*, 59, 1-7, 10.1111/j.1469-8137.1960.tb06195.x, 1960.

728 Wilson, J. W.: Analysis of the spatial distribution of foliage by two-dimensional point quadrats, *New Phytol.*, 58, 92-99,  
729 <https://doi.org/10.1111/j.1469-8137.1959.tb05340.x>, 1959.

730 Xiao, Q., McPherson, E. G., Ustin, S. L., and Grismer, M. E.: A new approach to modeling tree rainfall interception, *Journal*  
731 *of Geophysical Research: Atmospheres*, 105, 29173-29188, 2000.

732 Yan, G., Jiang, H., Luo, J., Mu, X., Li, F., Qi, J., Hu, R., Xie, D., and Zhou, G.: Quantitative Evaluation of Leaf Inclination  
733 Angle Distribution on Leaf Area Index Retrieval of Coniferous Canopies, *Journal of Remote Sensing*, 2021, 1-15,  
734 10.34133/2021/2708904, 2021.

735 Yan, K., Wang, J., Peng, R., Yang, K., Chen, X., Yin, G., Dong, J., Weiss, M., Pu, J., and Myneni, R. B.: HiQ-LAI: a high-  
736 quality reprocessed MODIS leaf area index dataset with better spatiotemporal consistency from 2000 to 2022, *Earth System*  
737 *Science Data*, 16, 1601-1622, 10.5194/essd-16-1601-2024, 2024.

738 You, N., Dong, J., Huang, J., Du, G., Zhang, G., He, Y., Yang, T., Di, Y., and Xiao, X.: The 10-m crop type maps in  
739 Northeast China during 2017-2019, *Sci Data*, 8, 41, 10.1038/s41597-021-00827-9, 2021.

740 Zhang, X., Yan, K., Liu, J., Yang, K., Pu, J., Yan, G., Heiskanen, J., Zhu, P., Knyazikhin, Y., and Myneni, R. B.: An Insight  
741 Into the Internal Consistency of MODIS Global Leaf Area Index Products, *IEEE Transactions on Geoscience and Remote*  
742 *Sensing*, 62, 1-16, 10.1109/tgrs.2024.3434366, 2024.

743 Zhao, J., Li, J., Liu, Q., Xu, B., Yu, W., Lin, S., and Hu, Z.: Estimating fractional vegetation cover from leaf area index and  
744 clumping index based on the gap probability theory, *International Journal of Applied Earth Observation and Geoinformation*,  
745 90, 102-112, 10.1016/j.jag.2020.102112, 2020.

746 Zheng, G. and Moskal, L. M.: Leaf orientation retrieval from terrestrial laser scanning (TLS) data, *IEEE Transactions on*  
747 *Geoscience and Remote Sensing*, 50, 3970-3979, 10.1109/TGRS.2012.2188533, 2012.

748 Zou, X. and Möttus, M.: Retrieving crop leaf tilt angle from imaging spectroscopy data, *Agricultural and Forest Meteorology*,  
749 205, 73-82, 10.1016/j.agrformet.2015.02.016, 2015.

750 Zou, X., Möttus, M., Tammeorg, P., Torres, C. L., Takala, T., Pisek, J., Mäkelä, P., Stoddard, F. L., and Pellikka, P.:  
751 Photographic measurement of leaf angles in field crops, *Agricultural and Forest Meteorology*, 184, 137-146,  
752 10.1016/j.agrformet.2013.09.010, 2014.

753

754